arXiv:2506.14041v1 [astro-ph.CO] 16 Jun 2025

Hawking Radiation Signatures from Primordial Black Holes Transiting the Inner Solar System: Prospects for Detection

Alexandra P. Klipfel [1,*] Peter Fisher,[1,†] and David I. Kaiser [1,‡]

[1]*Department of Physics, Massachusetts Institute of Technology, Cambridge, MA 02139, USA*

(Dated: June 18, 2025)

Primordial black holes (PBHs) arise from the collapse of density perturbations in the early universe and serve as a dark matter (DM) candidate and a probe of fundamental physics. There remains an unconstrained "asteroid-mass" window where PBHs of masses $10^{17}\text{g} \lesssim M \lesssim 10^{23}\text{g}$ could comprise up to 100% of the dark matter. Current $e^{\pm}$ Hawking radiation constraints on the DM fraction of PBHs are set by comparing observed spatial- and time-integrated cosmic ray flux measurements with predicted Hawking emission fluxes from the galactic DM halo. These constraints depend on cosmic ray production and propagation models, the galactic DM density distribution, and the PBH mass function. We propose to mitigate these model dependencies by developing a new local, time-dependent Hawking radiation signature to detect low-mass PBHs transiting through the inner Solar System. We calculate transit rates for PBHs that form with initial masses $M \lesssim 5 \times 10^{17}\text{g}$. We then simulate time-dependent positron signals from individual PBH flybys as measured by the Alpha Magnetic Spectrometer (AMS) experiment in low-Earth orbit. We find that AMS is sensitive to PBHs with masses $M \lesssim 2 \times 10^{14}\,\text{g}$ due to its lower energy threshold of $500\,\text{MeV}$. We demonstrate that a dataset of daily positron fluxes over the energy range $5 - 500\,\text{MeV}$, with similar levels of precision to the existing AMS data, would enable detection of PBHs drawn from present-day distributions that peak within the asteroid-mass window. Our simulations yield $\mathcal{O}(1)$ detectable PBH transits per year across wide regions of parameter space, which may be used to constrain PBH mass functions. This technique could be extended to detect γ-ray and X-ray Hawking emission to probe further into the asteroid-mass window.

I. INTRODUCTION

Primordial black holes (PBH) are theorized to form from the collapse of primordial density perturbations in the early universe. Those that form with sufficient initial mass, $M_i \gtrsim 5.34 \times 10^{14}\,\text{g}$, would persist to the present day and contribute to the dark matter (DM) density Ω_{DM} [1–7]. Various cosmological models predict the existence of PBHs over a wide present-day mass range which, in principle, could span approximately 40 orders of magnitude, from $10^{14}\,\text{g}$ to $10^{55}\,\text{g}$ [7–12]. This translates to $10^{-19} M_\odot \lesssim M \lesssim 10^{22} M_\odot$. Despite many experimental constraints on the PBH dark matter fraction f_{PBH}, there remains an open "asteroid-mass" window within which PBHs of mass $10^{17}\,\text{g} \lesssim M \lesssim 10^{23}\,\text{g}$ may comprise up to 100% of the cold dark matter (CDM) [7–15]. We are motivated to experimentally search for PBHs not only because they could make up a significant fraction of the dark matter, but because the presence or absence of PBHs in our universe, even for $f_{\text{PBH}} \ll 1$, can allow us to constrain cosmological models and to probe fundamental and beyond-Standard-Model (BSM) physics.

Studying PBHs within the framework of individual transit events through our Solar System provides unique opportunities to constrain the PBH dark matter fraction, directly observe low-mass PBHs, and detect Hawking radiation. In this article we investigate the feasibility of using Hawking emission from PBHs transiting through the inner Solar System to constrain the PBH dark matter fraction for $M \lesssim 5 \times 10^{17}$ g. We investigate whether a time-dependent positron emission signature from a PBH transiting within approximately $10^{-3} - 10\,\text{AU}$ of the Earth would be detectable with the Alpha Magnetic Spectrometer (AMS) experiment, a cosmic ray observatory mounted on the International Space Station (ISS) [16], or with realistic next-generation detectors. We also discuss the possibility of performing similar analyses with high-energy photons and $e^{\pm}$ datasets from various other telescopes, cosmic ray observatories, and solar probes. This new time-dependent PBH transit signature is valuable, because it is model-independent and could be extended to X-ray and low-energy positron datasets to probe far into the asteroid-mass window.

Upon developing a matched-filter pipeline to extract time-dependent Hawking emission signals from simulated time-series AMS positron data, we find that the existing AMS experiment is only sensitive to transiting PBHs with masses $M \lesssim 2 \times 10^{14}\,\text{g}$. As discussed below, such a value is well below the present lower-bound for which PBHs could constitute a significant fraction of the DM abundance today. The positron energy range to which the AMS experiment is sensitive ($Q \geq Q_{\text{min}} = 500\,\text{MeV}$) is limited by the strong effects of the geomagnetic field for detectors (like AMS) in low-Earth orbit. We show that realistic detectors with AMS-like precision positioned at higher altitudes, or even at a Lagrange point, could reliably detect positrons with $Q \geq Q_{\text{min}} = 5\,\text{MeV}$. Such instruments would be capable of directly detecting several PBH transits per year, or—in the absence of any such detections—of placing strong constraints on a large set of PBH mass functions.

Following a brief discussion of the motivation and current constraints on searches for Hawking radiation from PBHs, in Sec. II we introduce various models and parameterizations for Hawking emission, PBH mass distributions, the lo-

* aklipfel@mit.edu
† fisherp@mit.edu
‡ dikaiser@mit.edu

cal DM density distribution, and detector characteristics. Section III discusses expected transit rates for positron-producing PBHs in the inner Solar System, simulation results for time-dependent positron Hawking emission signatures from PBH transits, and prospects for detecting PBHs and/or constraining PBH mass functions with existing and hypothetical future datasets. Concluding remarks follow in Sec. IV.

A. Motivation

Primordial black holes garnered new attention as a dark matter candidate over the last decade in the wake of LIGO-Virgo-KAGRA (LVK) collaboration data and James Webb Space Telescope (JWST) observations. Some physicists [17, 18] have interpreted gravitational-wave signatures from binary black hole mergers with candidates in the lower [19] and pair-instability [20] mass gaps as potential PBH candidates. Additionally, several analyses of public LVK data claim to observe sub-solar mass black holes [21, 22], which would be excellent PBH candidates. The LVK collaboration, however, reports no such candidates with sufficient significance in their second and third observing runs [23, 24]. Furthermore, JWST observations of galaxies [25–30] and candidate active galactic nuclei (AGN) [31–35] with redshift $z \gtrsim 10$ are in tension with the ΛCDM standard model of cosmology [36]. These observations have reinvigorated interest in PBHs as seeds for early galaxies and the supermassive black holes at the centers of their AGNs [37–40].

The ΛCDM model predicts that about 26% of the energy density of the universe is comprised of non-relativistic, non-baryonic matter with extremely weak coupling to Standard Model particles [41]. Whereas the evidence for the existence and relative fraction of DM is very strong, as yet there does not exist any decisive evidence to support various DM particle candidates, such as axions, axion-like particles, weakly interacting massive particles (WIMPs), or sterile neutrinos [42–46]. Primordial black holes also satisfy the ΛCDM dark matter criteria, and their formation and properties can be explained entirely within current theories of general relativity, ΛCDM, inflation, and the Standard Model. Most models predict that PBHs formed before baryogenesis and thus contribute to the non-baryonic dark matter density $\Omega_{\rm DM}$ rather than to the baryonic density Ω_b—which can be at most 5% of the critical energy density [9]. Because PBHs with masses within the asteroid-mass range (or larger) are expected to be uncharged under any Standard Model gauge group in the present-day epoch [47, 48], they can only interact gravitationally with SM particles. Furthermore, due to their large masses, PBHs are inherently non-relativistic—"cold"—objects capable of coalescing to form large-scale structures in the universe.

Primordial black holes also provide a useful tool with which to investigate cosmological history. Proposed PBH formation mechanisms include the collapse of primordial over-densities, pressure reduction in the QCD epoch, cosmic phase transitions and domain-wall collapse, self-intersection of cosmic strings, bubble collisions, and collapse of a scalar field. (See Refs. [7, 11–13] for a thorough discussion of possible PBH formation processes.) The parameters of a specific cosmological model determine the shape of the present-day PBH number density distribution, dn/dM, and the fraction of DM comprised of PBHs, $f_{\rm PBH} = \Omega_{\rm PBH,0}/\Omega_{\rm DM,0}$. Working backward from experimental constraints on $f_{\rm PBH}$, we can constrain cosmological models and probe the physics of the early universe and the shape of the primordial power spectrum.

Even if $f_{\rm PBH} \ll 1$, primordial black holes can serve as a useful probe of BSM physics. Studies of mixed dark matter scenarios, in which PBHs and one or more additional candidates comprise all the dark matter, place strong—nearly mutually exclusive—constraints on WIMPs in the GeV-TeV mass range for a wide range of PBH masses and DM fractions [9]. Mixed DM scenarios with axion-like particles [49] or sterile neutrinos [50] may also admit mutual constraints on these particle DM candidates and PBHs.

Perhaps most importantly, observation of low-mass PBHs may be the only viable method to directly detect Hawking radiation [51, 52], which is widely accepted as a theoretical triumph due to its unification of statistical mechanics, quantum field theory, and general relativity into a semi-classical framework. Black holes with masses larger than that of the Earth, $M \gtrsim M_\oplus \approx 10^{27}\,\mathrm{g}$, emit only photons and neutrinos with temperatures significantly below $2.7\,\mathrm{K}$ and $1.9\,\mathrm{K}$, respectively. Therefore, Hawking radiation from all known stellar and supermassive black holes will be hidden by the Cosmic Microwave Background (CMB) and Cosmic Neutrino Background (CνB). However, the existence of PBHs with masses $M \ll M_\oplus$—even if $f_{\rm PBH} \ll 1$—would provide an opportunity to directly detect Hawking emission of photons, neutrinos, and $e^\pm$. Recent work also posits that extremely low-mass PBHs may emit heavier stable particles at detectable rates, including isotopes of hydrogen and helium nuclei [53]. Detecting Hawking radiation is among the only experimental probes with which physicists can investigate a possible unification of quantum field theory and general relativity at achievable energy scales.

B. Evaporation Constraints

Across their entire mass range, PBHs should interact with known matter in predictable ways. These interactions manifest as observational signatures, which can be used to directly detect PBHs or to place constraints on $f_{\rm PBH}$. Potential signatures include Hawking emission, accretion, dynamical effects, large-scale structure formation, gravitational lensing, and gravitational waves. See Refs. [7–15] for a thorough review of current constraints from these signatures and others. We are interested in developing a new PBH detection signature and the requisite data analysis techniques to probe the open asteroid-mass window, $10^{17}\,\mathrm{g} \leq M \leq 10^{23}\,\mathrm{g}$. Reaching this notoriously inaccessible PBH mass range requires the development of novel signatures because these black holes have Schwarzschild radii, $R_s \equiv 2GM/c^2$, smaller than a micron, thus rendering known gravitational lensing techniques to be much more difficult to apply.

The black holes we discuss in this article have initial

formation-time masses 5.34×10^{14} g $\leq M_i \leq 5 \times 10^{17}$ g, a window we refer to as the "$e^{\pm}$-production mass range," which corresponds to radii between approximately $1 - 1000\,\mathrm{fm}$. We are focusing our initial efforts on positron Hawking emission, and therefore on PBHs with present-day masses $M \leq 5 \times 10^{17}$ g, because positrons have low astrophysical backgrounds and the AMS-02 experiment has a large acceptance and provides over a decade of high-precision time-series positron flux data.

Hawking radiation provides useful *evaporation constraints* on the dark matter fraction of low-mass PBHs with $M \lesssim 10^{17}$g. Hawking's semi-classical formulation of black hole evaporation [51, 52] predicts that a PBH should emit all SM particles during the course of its lifetime. PBHs that form within the $e^{\pm}$-producing range, $5.34 \times 10^{14} \leq M_i \leq 5 \times 10^{17}$ g, will emit photons, neutrinos, light charged leptons, and pions peaking in the MeV-GeV energy range, while PBHs in the asteroid-mass window will emit photons and neutrinos peaking in the eV-MeV range. PBHs at the very end of their lives will rapidly lose their remaining mass and effectively explode by emitting high fluxes of all 17 Standard Model particles—including heavy hadrons, leptons, and massive bosons. For example, as discussed in section II B 2, a PBH with mass $M_* \equiv 5.34 \times 10^{14}$ g has a lifetime equal to the current age of the universe, while a PBH with mass 6×10^{10} g has a lifetime of approximately 1 day and a temperature $T \approx 176\,\mathrm{GeV}$, which is hot enough to emit top quarks and Higgs bosons. PBH explosions could also be sources of ultra-high-energy cosmic rays [54–58] and heavy antimatter cosmic rays [53].

Evaporation constraints in the literature from present-epoch Hawking radiation are split into two categories: γ-ray constraints and $e^{\pm}$ constraints. The methodology behind these constraints is to exclude all PBH mass-functions for which a galactic PBH population would produce particle fluxes that exceed the observed galactic (and extragalactic) time- and spatially-integrated cosmic ray backgrounds. Current $e^{\pm}$ Hawking emission constraints are derived from time-independent Voyager-1 data and Alpha Magnetic Spectrometer (AMS) data [59–62]. Due to the uncertainties associated with galactic cosmic ray propagation models and our current limited understanding of the e^{+} background, we seek to develop a new, local signature of PBH Hawking emission that does not rely so heavily on these models.

Searching for PBHs that transit through our Solar System allows us to be agnostic about PBH mass functions and galactic cosmic ray propagation models and affords an opportunity to make a direct detection of Hawking radiation. Previous literature proposes that detecting Hawking radiation [63, 64] or orbital perturbations [65–67] from PBHs in our Solar System may be viable detection strategies. In this article, we simulate the observed time-dependent positron fluxes from PBHs transiting between $\sim 0.01 - 10\,\mathrm{AU}$ of the Earth and investigate whether such transits could be detected by the AMS-02 experiment aboard the ISS. We predict the PBH mass functions that could be constrained with current AMS data and with possible future cosmic ray positron datasets. Furthermore, the method of detecting time-dependent Hawking radiation signatures from local transits developed here can be generalized to γ-ray, X-ray, and low-energy positron datasets, which would allow us to probe PBHs with masses up to $\sim 10^{20}$ g—a mass range unreachable by current evaporation constraint techniques based on isotropic galactic and extragalactic cosmic ray fluxes.

Orbital perturbation signatures are most sensitive to the heaviest PBHs in the asteroid-mass range, while the proposed Hawking emission signatures discussed here are most sensitive to the lighter end of this window, where the PBHs are hotter emitters. Thus, these two novel signatures combined have the potential to probe the entirety of the asteroid-mass window, and to possibly make a direct detection of a PBH candidate or to place strong constraints on the PBH DM fraction.

II. MODELS

A. Hawking Radiation

Hawking radiation [51, 52, 68–70] is not limited to the emission of massless particles. Provided that a black hole is small enough and therefore hot enough, it can emit all 17 Standard Model particles as fundamental degrees of freedom. These fundamental emission rates are referred to as *primary emission spectra*. To determine the feasibility of detecting Hawking radiation from primordial black holes transiting past Earth with space-based cosmic ray experiments like AMS, we must accurately simulate the PBH emission spectra for photons, electrons, and positrons. Because our technique probes hot, low-mass PBHs, it is critical that we account for QCD jets, hadronization, and particle decays associated with the primary emission of quarks, muons and other short-lived particles [71]. Jet fragmentation and particle decays will contribute to the net emission rates—referred to as *secondary emission spectra*—of stable, detectable fundamental and composite particles. We therefore will use secondary rather than primary emission spectra throughout our analysis.

1. *Primary Emission*

A black hole of mass M, angular velocity Ω, electric potential Φ, and surface gravity κ will emit fundamental particles of species j at a rate [68, 71]:

$$\frac{d^2 N_j^{(1)}}{dt dQ} = g_j \frac{\Gamma_{s_j}}{2\pi\hbar} \left[\exp\left(\frac{Q - n\hbar\Omega - q\Phi}{\hbar\kappa/2\pi c} \right) - (-1)^{2s_j} \right]^{-1} \tag{1}$$

where the particle has spin s, angular momentum $n\hbar$, charge q, energy Q, and total quantum degrees of freedom g. The quantity in Eq. (1) is called the *primary emission spectrum* for a given particle species. (See the Supplemental Materials of Ref. [56] for appropriate g parameters for all SM particles.) To compute the primary emission spectrum of positrons, for example, we must use $g = 2$ to account for the two helicity degrees of freedom. The bracketed term on the right hand side

of Eq. (1) has the form of a blackbody spectrum for an emitter at temperature

$$T = \frac{\hbar\kappa}{2\pi k_B c}. \tag{2}$$

The important physics enters through the *greybody factor*, Γ_s, a dimensionless quantity which is generally a function of the black hole parameters Ω, Φ, M, and κ and the particle parameters Q, m, and s. The greybody factor is defined in terms of the absorption cross section σ_s associated with scattering a Standard Model field of mass m and spin s off a black hole of mass M in curved spacetime [71]:

$$\Gamma_s(M, Q, m) = \frac{\sigma_s(M, Q, m)}{\pi\hbar^2 c^2}(Q^2 - m^2). \tag{3}$$

A simplified form of Eq. (3) holds exactly for massless particles and approximately for relativistic massive particles:

$$\Gamma_s(M, Q) = \frac{\sigma_s(M, Q)}{\pi\hbar^2 c^2}Q^2. \tag{4}$$

(For a perfect blackbody, $\Gamma_s = 1$.) Note that under the relativistic assumption of Eq. (4), the emission spectra of massive particles must be cut off at $Q = m$. MacGibbon and Webber [71] remark that the relativistic form of Γ_s in Eq. (4) only differs notably from the exact non-relativistic result for $Q \leq 2m$, and never by more than 50%. We thus conclude that the cutoff at $Q = m$ dominates calculations of total emission rates and we can employ the relativistic approximation of Γ_s for all $Q > m$. The calculation of greybody factors for Schwarzschild black holes is discussed in detail in Refs. [68, 71–73].

Because we only consider non-rotating and uncharged Schwarzschild black holes, we take $\Omega = \Phi = 0$ and

$$k_B T = \frac{\hbar c^3}{8\pi G M}. \tag{5}$$

Assuming also that Γ_s takes the form of Eq. (4), the primary emission spectrum for particle species j reduces to:

$$\frac{d^2 N_j^{(1)}}{dt dQ} = g_j \frac{\Gamma_{s_j}}{2\pi\hbar}\left[\exp\left(\frac{Q}{\hbar c^3/8\pi G M}\right) - (-1)^{2s_j}\right]^{-1}. \tag{6}$$

The assumption that primordial black holes are uncharged and non-rotating is a reasonable one. Page [69] showed that an initially rotating black hole will preferentially emit particles with spin aligned with the hole's angular momentum, causing it to "spin down" to within 1% of the emission rate a Schwarzschild configuration before half of its energy is radiated away. He further demonstrates that an initially maximally rotating PBH will only have a lifetime 2.32 times longer than its Schwarzschild counterpart [69]. Page thus concludes that it is valid to assume decaying black holes have negligible rotation [69]. In addition, PBHs generally form with $\Omega = 0$ from the collapse of spherically symmetric scalar perturbations, and, due to negligible accretion rates, PBHs within the asteroid-mass range will not spin up over time [74–76]. Furthermore, PBHs discharge any initial charge even more efficiently than they lose angular momentum [47, 77], leaving tiny, stochastic charge fluctuations of order $\mathcal{O}(e) \ll \sqrt{G}M$ [70, 78].

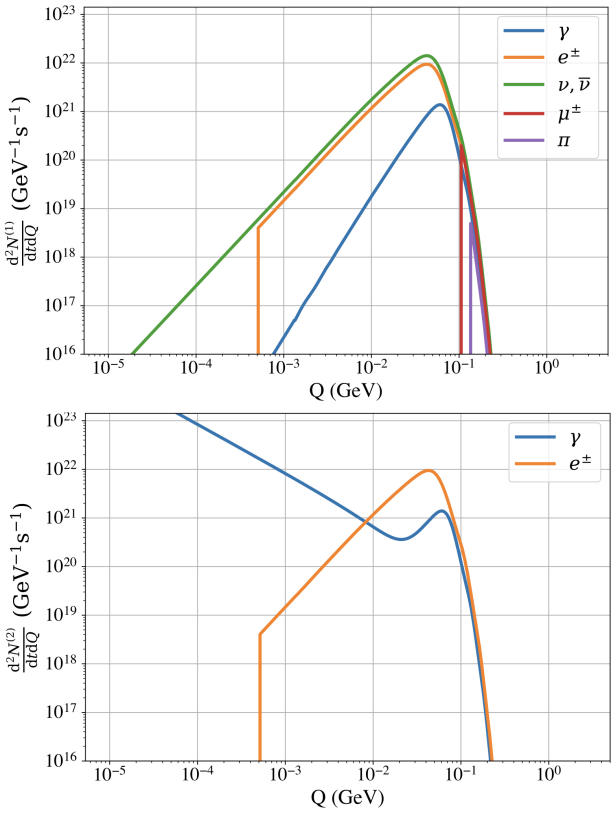


Figure 1: Primary (top) and secondary (bottom) Hawking emission spectra for a primordial black hole with mass $M = 10^{15}$g. Spectra are calculated numerically with `BlackHawk v2.2` [79, 81] and `hazma` [82] following the discussions in Sections II A 1 and II A 2. Note that no secondary p or $\bar{p}$ appear because these rates are negligible given $T = 10.6\,\text{MeV} \ll m_p$. Fermion spectra shown are the sum of particle and antiparticle emission rates. The primary neutrino spectra are summed over all flavors. No secondary neutrino spectra are shown because such processes are not incorporated within the `hazma` code.

We therefore assume all PBHs are Schwarzschild and use Eq. (6) to compute primary emission spectra for all 17 fundamental Standard Model particles. The calculation of primary spectra is done numerically via the open source Hawking radiation code `BlackHawk v2.2`, which makes equivalent assumptions [79, 80].

2. *Secondary Emission*

Due to their stability, electrons, positrons, photons, neutrinos, protons, and antiprotons provide the only measurable signatures of Hawking radiation from a PBH transiting past

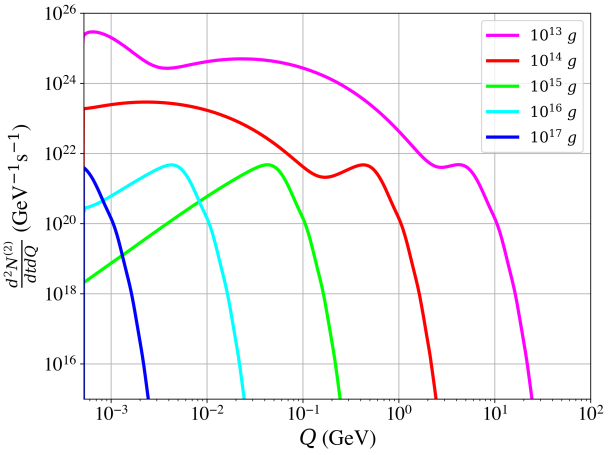


Figure 2: Secondary positron emission spectra for PBHs in the positron-producing mass range. Note that the x-axis plots total positron energy Q and thus cuts off at the rest mass $Q = 0.511$ MeV. PBHs with masses $M \gtrsim 10^{14}$ g have secondary spectra well-approximated by their primary spectra because they emit few short-lived heavier particles.

a detector with an impact parameter on the order of an astronomical unit (AU). We note that PBHs should, in principle, produce additional long-lived particles during the final explosive phase of their lives, including isotopes of hydrogen and helium and their anti-nuclei in equal numbers [53].

The total emitted fluxes of stable particles, referred to as *secondary emission spectra*, have contributions from their individual primary emission spectra (if the particles are fundamental), from decays of unstable primary particles, and from the hadronization and fragmentation of quark-gluon jets. This approach was pioneered by MacGibbon and Webber [71], who argued that a black hole will emit primary particles which appear elementary at its temperature scale and that these primary particles will form composite particles and decay to stable, detectable secondary particles.

The secondary emission spectrum for particle species i is calculated via:

$$\frac{d^2N_i^{(2)}}{dtdQ} = \int_0^\infty \sum_j \frac{d^2N_j^{(1)}}{dtdQ'} \frac{dN_i^j}{dQ} dQ', \tag{7}$$

where we sum over all primary Hawking particles j and weight by the differential branching ratios $dN_i^j(Q', Q)/dQ$ [79].

The numerical calculation of secondary emission spectra is carried out with `BlackHawk v2.2` [79, 80], which implements the particle physics codes `PYTHIA` [83] and `hazma` [82] to compute the branching ratios N_i^j due to jets and decays. `PYTHIA` treats the emission of quarks and gluons as fundamental, and thus is only applicable for computing the secondary spectra of PBHs with masses $M \lesssim 10^{14}$ g, because such PBHs are hotter than the QCD scale (approximately 200 MeV). Within the mass range $M \gtrsim 10^{14}$ g , PBHs are too cold to emit quarks directly, since such quarks would be at energies below the pion rest mass, so for PBHs with masses in the range $10^{14}\,\mathrm{g} \lesssim M \lesssim 10^{17}\,\mathrm{g}$ we compute the secondary emission spectra with `hazma`, which treats pions as fundamental degrees of freedom and does not compute quark or gluon primary emission. For masses $M \gtrsim 10^{17}$g, secondary positron spectra from `PYTHIA` and `hazma` converge, and we use `PYTHIA` as our afterburner. We note that integrated positron fluxes computed with `PYTHIA` and `hazma` differ by at most a few percent for PBHs with $M \gtrsim 10^{14}$ g. The primary and secondary `hazma` spectra for a PBH with $M = 10^{15}$ g are shown in Fig. 1.

The secondary emission spectra are considered the *instantaneous* particle emission spectra from a PBH; but, in principle, these spectra are modulated by various energy-loss processes as the emitted particles propagate from the PBH to the detector. The positron flux as measured by a distant detector would be modified by processes including scattering off the interstellar (or interplanetary) medium, synchrotron radiation, photon pair-production, and bremsstrahlung. We ignore these "tertiary" contributions to the Hawking emission spectra due to the relatively short length scales, $\mathcal{O}(1\,\mathrm{AU})$, and low positron energy scales, $Q \lesssim 1\,\mathrm{GeV}$, considered here.

B. Distribution and Evolution of PBH Masses

Constraints on the PBH dark matter fraction $f_{\rm PBH}$ were originally derived assuming that all PBHs formed with some mass $\bar{M}$, thus obeying a "monochromatic" mass function, which is generally regarded as unphysical [84–86]. Instead, in this section we introduce more realistic extended PBH mass functions, which incorporate physical features of the process by which PBHs form. Moreover, the PBH mass function will evolve over time, as individual PBHs undergo Hawking evaporation. Hence it is imperative to evolve such mass functions to the present day when evaluating constraints on $f_{\rm PBH}$. The time-evolution of the PBH mass function inevitably introduces a power-law tail for small masses, independent of whether the mass function at the time of PBH formation included such a feature. Incorporating such extended mass functions yields a modest tightening of constraints on the asteroid-mass window [10, 15, 84, 85].

1. PBH Mass Functions

At the time t_i of PBH formation, the normalized PBH differential mass density function $\psi(M_i)$, referred to as the *mass function*, is defined in relation to the differential number density distribution $dn_{\rm PBH}/dM$ via

$$\psi(M_i) = \frac{1}{\rho_{{\rm PBH},i}} \frac{d\rho_{{\rm PBH},i}}{dM_i} = \frac{M_i}{\rho_{{\rm PBH},i}} \frac{dn_{{\rm PBH},i}}{dM_i}, \tag{8}$$

where $\psi(M_i)$ satisfies $\int dM_i\, \psi(M_i) = 1$ and determines the shape of the initial distribution. Here $n_{{\rm PBH},i}$ is the comoving PBH number density at formation time.

PBHs form from the gravitational collapse of primordial curvature perturbations, in a process known as "critical collapse" [87–91]. Upon re-entering the Hubble radius, perturbations with amplitude above a critical threshold will induce collapse, with the resulting PBH mass given by

$$M_i = \kappa M_H(t_i)|\bar{\mathcal{C}} - \mathcal{C}_c|^\nu, \tag{9}$$

where $M_H(t_i)$ is the mass contained within a Hubble volume at time t_i, $\mathcal{C} = 2G\delta M(r)/r$ is the compaction as a function of areal radius r [92, 93], $\bar{\mathcal{C}}$ is the spatial average of the compaction over a Hubble radius, $\mathcal{C}_c \simeq 0.4$ is the threshold for PBH formation [94, 95], and κ is an $\mathcal{O}(1)$ dimensionless constant whose value depends on the spatial profile of $\mathcal{C}(r)$ and on the averaging procedure [96]. The universal scaling exponent ν depends on the equation of state of the fluid that undergoes collapse; numerical studies find $\nu = 0.36$ for a radiation fluid [88, 89, 91, 96].

Equation (9) implies that PBHs can form with arbitrarily small masses, if the (averaged) compaction is close to the critical threshold. Meanwhile, causality restricts PBHs to form with masses no larger than the Hubble mass at the time of formation. In fact, the typical mass at the peak of the distribution at the time of formation satisfies $\bar{M}(t_i) \simeq 0.2\, M_H(t_i)$ [97–100]. These features of the critical collapse process generically yield PBH mass distributions that have a power-law tail for masses $M_i < \bar{M}(t_i)$ and an exponential cut-off for masses $M_i \gtrsim \bar{M}(t_i)$.

Ref. [86] finds that these features of the PBH formation process are most accurately captured by the generalized critical collapse (GCC) parameterization of the PBH mass function. The normalized GCC mass function is defined as

$$\psi_{\rm GCC}(M_i|\mu,\alpha,\beta) = \frac{\beta}{\mu}\frac{1}{\Gamma((\alpha+1)/\beta)}\left(\frac{M_i}{\mu}\right)^\alpha \exp\left[-\left(\frac{M_i}{\mu}\right)^\beta\right], \tag{10}$$

where μ is a location parameter with dimensions of mass, $\alpha > 1$ controls the power-law scaling of the low-mass tail, and $\beta > 0$ controls the high-mass exponential cutoff. The GCC mass function peaks at

$$\bar{M}_{\rm GCC}(\mu,\alpha,\beta) = \mu\left(\frac{\alpha}{\beta}\right)^{1/\beta}. \tag{11}$$

The original critical-collapse (CC) mass function corresponds to $\alpha = \beta = \nu^{-1}$.

It has also been common in the literature to consider a simple log-normal (LN) distribution for the initial mass function [9, 15, 101]:

$$\psi_{\rm LN}(M_i|\mu,\sigma) = \frac{1}{\sqrt{2\pi}\sigma M_i}\exp\left[-\frac{\log\left(M_i/\mu\right)^2}{2\sigma^2}\right]. \tag{12}$$

This model depends on two parameters: μ, with dimensions of mass which sets the peak location of $M_i\psi(M_i)$, and σ, a dimensionless width parameter. The LN mass function

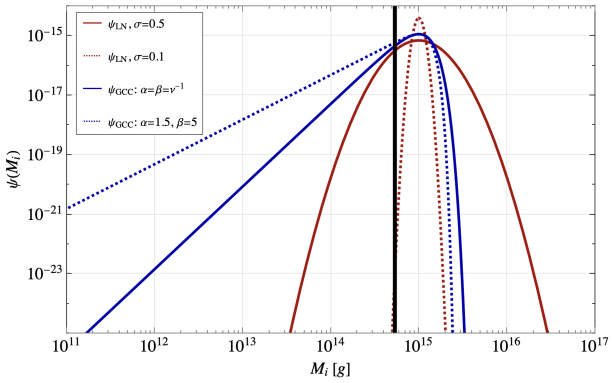


Figure 3: Comparison of GCC (blue) and LN (red) formation-time mass functions with peaks located at $\bar{M}(t_i) = 10^{15}\,$g. The vertical black line indicates the universe-lifetime cutoff mass M_* given in Eq. (22). The main difference between the two parameterizations is the presence or absence of the small-mass tail.

$\psi_{\rm LN}(M_i)$ peaks at mass

$$\bar{M}_{\rm LN}(\mu,\sigma) = \mu e^{-\sigma^2}. \tag{13}$$

Although the LN distribution depends on one fewer parameter than the GCC distribution, it omits the small-mass power-law tail, which comes directly from the critical-collapse relationship for M_i of Eq. (9). See Fig. 3. As we will see, the small-mass tail of the initial mass function can play an important role when considering detection prospects for Hawking emission from PBHs near the lower edge of the asteroid-mass range.

2. *PBH Mass Loss*

The mass of an individual PBH will evolve over time as it emits Hawking radiation [71, 102]:

$$\frac{dM}{dt} = -\sum_j g_j \int_{m_{{\rm eff},j}}^\infty dQ\,\frac{Q}{c^2}\frac{d^2N_j^{(1)}}{dtdQ} = -A\frac{f(M)}{M^2}, \tag{14}$$

where the sum is taken over all fundamental Standard Model particles, $d^2N_j^{(1)}/dtdQ$ is the primary Hawking spectrum for particle j, and $A = 5.19\times10^{25}\ {\rm g}^3\,{\rm s}^{-1}$.

The function $f(M)$, referred to as the *Page factor*, quantifies the total number of quantum degrees of freedom that can be emitted by a PBH of mass M. The value of A is chosen to normalize the Page factor such that $f(M) = 1$ for PBHs emitting only photons and neutrinos (which are treated as massless). We follow the method of Ref. [102] and define the Page

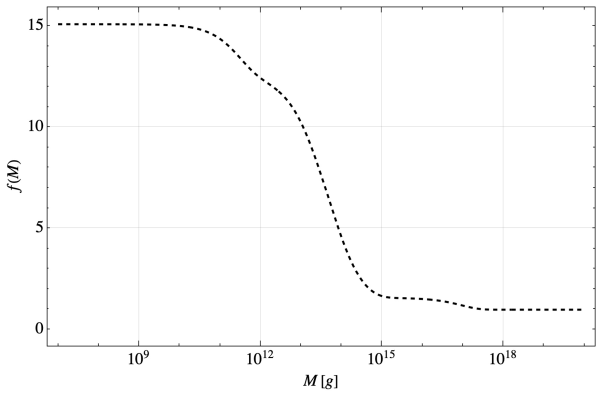


Figure 4: The Page factor $f(M)$ as a function of PBH mass as defined in Eq. (15). We have normalized the Page factor such that $f(M) = 1$ for PBHs emitting only photons and neutrinos, which are assumed massless. PBH mass M here indicates mass at time of particle emission.

factor as

$$f(M) \simeq \mathcal{P}_\gamma + \mathcal{P}_\nu + \sum_j \mathcal{P}_j \exp\left(-\frac{M}{M_j}\right), \tag{15}$$

where the Page coefficients $\mathcal{P}_j$ and the quantum degrees of freedom (DOF) g_j can be found in Table 2 of the Supplemental Materials of Ref. [56]. The characteristic mass M_j is defined as the PBH mass at which the emitted power for species j peaks at the effective particle mass $m_{\mathrm{eff},j}$. Note that, unlike Ref. [102], we include terms for the W, Z, and Higgs bosons and use updated particle masses. The inclusion of the exponential factors in $f(M)$ is a phenomenological way to smoothly ramp up the total number of DOF as particle production "turns on" for each new species when $T \approx m_{\mathrm{eff},j}$. The Page factor is plotted in Fig. 4.

We can write down an approximate analytical solution to Eq. (14) by solving the equation

$$\int \frac{M^2}{f(M)} dM = -\int A\, dt + C, \tag{16}$$

where C is an integration constant. We integrate by parts on the right-hand side:

$$\begin{aligned}\int \frac{M^2}{f(M)} dM &= \frac{1}{3}\frac{M^3}{f(M)} - \int \frac{1}{3} M^3 \frac{d}{dM} f(M)^{-1} dM \\ &= \frac{1}{3}\frac{M^3}{f(M)} + \int \frac{1}{3}\frac{M^3}{f(M)^2}\frac{df(M)}{dM} dM \\ &\approx \frac{1}{3}\frac{M^3}{f(M)},\end{aligned} \tag{17}$$

where we have used the assumption that $f(M)$ varies slowly—i.e., that $df(M)/dM \approx 0 \,\forall\, M$. This assumption holds within the regime of interest to us because the second term on the right-hand side of the second line of Eq. (17) is at least an order of magnitude smaller than the first for all masses $M \geq 10^{12}$ g.

Upon using the initial condition $M(t_i = 0) = M_i$, we then recover a relation between M and M_i at time t:

$$\frac{1}{f(M)} M^3 = -3At + \frac{1}{f(M_i)} M_i^3. \tag{18}$$

It is common to make the further assumption that $f(M) = f(M_i)$, which allows one to solve directly for $M(t)$ [103]:

$$M(t, M_i) \approx \left(-3A f(M_i) t + M_i^3\right)^{1/3}, \tag{19}$$

for its inverse:

$$M_i(t, M) \approx \left(3A f(M) t + M^3\right)^{1/3}, \tag{20}$$

and for the approximate PBH lifetime [4, 102]:

$$\tau(M_i) \approx \frac{1}{3A}\frac{M_i^3}{f(M_i)}. \tag{21}$$

However, for $M_i \sim M_*$ we see that $f(M_0) \approx 10 f(M_i)$, which implies that this assumption breaks down and Eqs. (19)–(21) become inaccurate for initial masses near M_*. (Note that M_0 indicates the present-day mass.) A more accurate result for $M(t, M_i)$ can be obtained by numerically solving Eq. (18) using $f(M)$ as defined in Eq. (15). Solving numerically for the value of M_i such that $M(t_0, M_i) = 0$, where the present age of the universe is $t_0 \equiv 13.787 \pm 0.020$ Gyr [41], gives the universe-lifetime cutoff mass:

$$M_* = 5.34 \times 10^{14}\,\mathrm{g}. \tag{22}$$

PBHs that form with $M_i = M_*$ would just be completing their Hawking evaporation process today.

3. *Present-Day Mass Functions*

The simplest way to construct an approximate present-day PBH mass function is to truncate the formation-time mass function $\psi(M_i)$ for $M_i \leq M_*$. Assuming that all PBHs with $M_i < M_*$ have evaporated, one could then define a present-day mass function $\psi(M, t_0)$ via $\psi(M, t_0) \propto \psi(M_i)\,\Theta(M_i - M_*)$, where $\Theta(x)$ is the Heaviside step function. Such a distribution could be normalized by requiring $\int_{M_*}^{\infty} dM\, \psi(M, t_0) = 1$. In practice, for PBH mass functions that peak at $\bar{M} \gg M_*$, one may neglect the evolution of the PBH population over time and simply set $\psi(M_i) \simeq \psi(M)$, which is commonly done in the literature.

However, for mass functions that are peaked near the lower-mass end of the asteroid-mass range and that have extended small-mass tails, this truncation procedure is insufficient to accurately describe the present-day PBH distribution. Such a procedure would neglect a real population of PBHs with masses below the cutoff M_* today, which exist due to mass-loss by heavier PBHs over cosmological timescales. To accurately model present-day mass functions that peak near the asteroid-mass range, we must therefore use the mass-loss for-

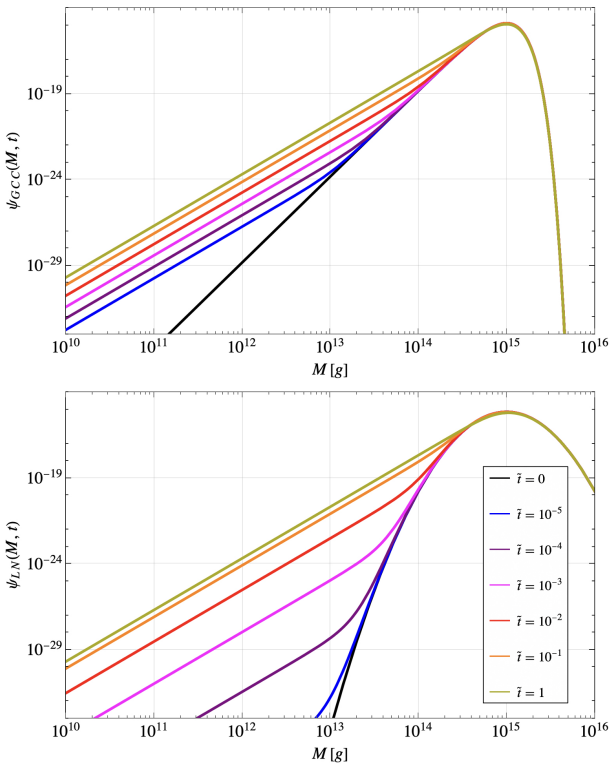


Figure 5: Time-evolution of the mass function $\psi_{\rm GCC}(M,t)$ with $\alpha = 5$ and $\beta = 2$ (top) and $\psi_{\rm LN}(M,t)$ with $\sigma = 0.5$ (bottom). Both functions are peaked at $\bar{M}_i = 10^{15}\,$g. The curves are plotted for different times $\tilde{t}$ in units of the current age of the universe, so that $\tilde{t} = 1$ corresponds to the present day.

malism discussed in Section II B 2 to evolve the formation-time mass functions to the present day [15, 54, 56, 103–105].

We first introduce the normalized *PBH number distribution function* [103, 105]:

$$\phi(M_i) \equiv \frac{1}{n_{\rm PBH,i}} \frac{dn_{\rm PBH,i}}{dM_i}. \tag{23}$$

This function is defined such that $\phi(M_i)dM_i$ is the fraction of PBHs with mass M_i at formation time, and satisfies $\int dM_i\, \phi(M_i) = 1$.

We can derive an exact relation between ϕ and ψ by combining Eqs. (23) and (8):

$$\phi(M_i) = \mathcal{C}\frac{1}{M_i}\psi(M_i), \tag{24}$$

where

$$\mathcal{C} \equiv \left[\int_0^\infty \frac{dM_i}{M_i}\psi(M_i)\right]^{-1}. \tag{25}$$

The peak mass of the distribution, $\bar{M}$, is a good approximation for the normalization constant $\mathcal{C}$ for sharply-peaked distributions. Therefore, following Ref. [56] we can relate

$$\phi(M_i) \approx \frac{\bar{M}}{M_i}\psi(M_i), \tag{26}$$

where $\bar{M}$ is given by Eq. (11) or (13), depending on the form of the initial-time PBH mass function.

To derive a general expression for $\psi(M,t)$ at some time $t > t_i$, we take advantage of the conservation of the total number of PBHs within a certain mass bin in the present day. The number N of PBHs with mass in some range $[M_1, M_2]$, $M_1 > 0$, at time t is given by the integral over the function $\phi(M)$:

$$\begin{aligned} N &= n_{\rm PBH,i}\int_{M_1}^{M_2} dM\,\phi(M,t) \\ &= n_{\rm PBH,i}\int_{M_i(M_1,t)}^{M_i(M_2,t)} dM\,\phi(M(M_i,t),t_i)\left[\frac{dM}{dM_i}\right]^{-1}, \end{aligned} \tag{27}$$

where, in the second line, we implemented a time-dependent change of coordinates $M \to M_i$ defined by $M = M(M_i,t)$ with Jacobian $|dM/dM_i|$, which can be derived from Eq. (18). Equating the integrands allows us to define the time-dependent PBH number distribution function as

$$\phi(M,t) = \phi(M_i(M,t),t_i)\frac{dM_i(M,t)}{dM}, \tag{28}$$

where $M_i(M,t)$ is the inverse of our coordinate transformation $M(M_i,t)$. Note that we have introduced new notation to explicitly encode the time-dependence: $\phi(M)$ at time t is $\phi(M,t)$ and $\phi(M_i) \equiv \phi(M_i,t_i)$.

Ref. [103] uses Eq. (28) and the relation $M_i(M,t)$ defined in Eq. (20) as a coordinate transformation to derive an approximate analytical expression for $\phi(M,t)$:

$$\begin{aligned} \phi(M,t) \approx\, & M^2\phi\left(M_i(M,t),t_i\right) \\ & \times \left(M^3 + 3Atf(M_i(M,t))\right)^{-2/3}. \end{aligned} \tag{29}$$

We can then use Eqs. (24) and (28) to construct a general expression for the time-dependent mass function $\psi(M,t)$ [105]:

$$\psi(M,t) = \frac{M}{M_i(M,t)}\psi(M_i(M,t),t_i)\frac{dM_i(M,t)}{dM}. \tag{30}$$

Substituting Eq. (20) as before to construct an approximate form of the time-dependent mass function yields

$$\begin{aligned} \psi(M,t) \approx\, & \frac{M^3}{M_i(M,t)}\psi\left(M_i(M,t),t_i\right) \\ & \times \left(M^3 + 3Atf(M_i(M,t))\right)^{-2/3}. \end{aligned} \tag{31}$$

We will refer to Eqs. (29) and (31) as the *analytical approximations* for ϕ and ψ. Figure 5 plots the analytical approximations of $\psi_{\rm GCC}(M,t)$ and $\psi_{\rm LN}(M,t)$ at various times $\tilde{t} \equiv t/t_0$ for $\bar{M} = 10^{15}\,$g, with GCC parameters $\alpha = 5$ and $\beta = 2$ and

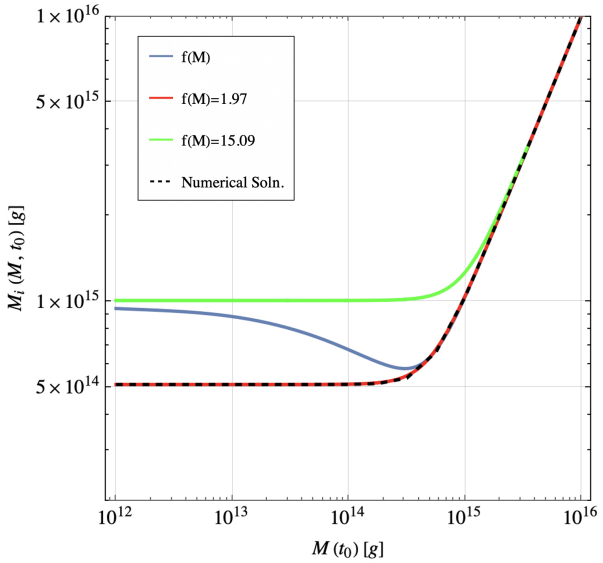


Figure 6: Approximate and exact numerical relations between formation-time mass M_i and present-day mass $M(t_0)$. The solid curves plot the approximate expression $M_i(M,t)$ from Eq. (20) with different assumptions for the Page Factor: explicit M-dependence according to Eq. (15) (blue), $f(M) = f(M_*) = 1.97$ (red), and $f(M) = \lim_{M\to 0} f(M) = 15.09$ (green). The dashed black curve is a numerical solution to Eq. (18) given the exact relation between M_i and M, which is very well approximated by setting $f(M) = f(M_*)$.

LN parameter $\sigma = 0.5$, where t_0 is the present age of the universe.

It's relevant to note that the approximate relations between M and M_i given by Eqs. (19) and (20), though convenient, result in an unphysical behavior in the mass evolution. Figure 6 plots $M_i(M,t)$ from Eq. (20) (blue), which does not display the monotonic behavior expected due to PBH evolution being "well-ordered" [105]. If two PBHs have masses M_1 and M_2 at time t_i satisfying $M_1 < M_2$, then we expect their masses to satisfy $M_1(t) < M_2(t)$ at any future time $t > t_i$—that is to say, that mass-ordering is preserved. Figure 6 shows the result from solving Eq. (18) numerically (black) and also plots Eq. (20) assuming that the Page factor is independent of mass: $f(M) = f(M_*) = 1.97$ (red) and $f(M) = \lim_{M\to 0} f(M) = 15.09$ (green). We find that (at least for masses $M(t_0) \geq 10^{12}$ g) it is a much better approximation of the true behavior to use $M_i(M,t)$ from Eq. (20) with $f(M) \approx 1.97$ than to include the mass-dependence of the Page factor.

All present-day mass functions used in this article are computed using Eq. (31) with $\psi(M_i, t_i)$ given by either Eq. (10) (GCC) or Eq. (12) (LN), and with $M_i(M,t)$ given by Eq. (20) with $f(M) = 1.97$ fixed.

As shown in Fig. 5, the present-time mass functions $\psi(M,t)$ feature power-law small-mass tails for both the GCC and LN distributions. In the GCC case, depending on the value of α, the small-mass tail of the time-evolved mass function can feature a more gentle slope than the formation-time mass function. More striking, the LN distribution develops a comparable small-mass tail to the GCC distribution over time, even though the formation-time LN distribution includes no such tail at all. When estimating detection rates for phenomena like cosmic rays emitted via Hawking emission from small-mass PBHs, it is therefore critical to time-evolve the PBH mass functions to the present day.

C. Local Dark Matter Distribution

The rate at which PBHs transit through the inner Solar System depends on the present-day PBH mass function, the local DM density, and the PBH velocity distribution relative to the Sun. In this section we discuss our assumptions for local PBH density and velocity distributions.

1. *Dark Matter Density Profile*

The visible Milky Way lies inside a large, approximately spherical dark matter halo [106, 107]. The DM density distribution of this halo $\rho_{\rm DM}(\vec{r})$ is established through galactic rotation curves, and is typically modeled as a Navarro-Frenk-White (NFW) profile [108], which is characterized by two parameters: a reference density ρ_0 and scale radius r_0.

We use the modified NFW-like density profile from Refs. [109, 110]:

$$\rho_{\rm DM}(r,z) = \frac{\rho_0}{L(1+L)^2}\exp\left[-\left(\frac{Lr_0}{r_{vir}}\right)^2\right], \tag{32}$$

where r and z are cylindrical coordinates in the Galactocentric frame and the best-fit parameters from Ref. [110] are:

$$L = \sqrt{\left(\frac{r}{r_0}\right)^2 + \left(\frac{z}{qr_0}\right)^2},$$

$$\begin{aligned} \rho_0 &= 0.0196\, M_\odot \mathrm{pc}^{-3}, \\ r_0 &= 15.5\,\mathrm{kpc}, \\ r_{vir} &= 287, \\ q &= 1.22. \end{aligned} \tag{33}$$

Other halo models in recent literature include a generalized Navarro-Frenk-White (gNFW) profile or the Einasto profile [111, 112].

The local dark matter density in the neighborhood of our Solar System, $\rho^{\odot}_{\rm DM}$, can be estimated by Jeans analysis of stellar motions [113] or by constructing galactic density models and rotation curves [111, 112, 114]. (See Ref. [115] for a review of local DM density measurements and techniques.) Measured values for $\rho^{\odot}_{\rm DM}$ generally fall between $0.2 - 1.5$ GeV/cm^3 [115]. Evaluating Eq. (32) at the location of the Solar System, $r_\odot = 8.3\,\mathrm{kpc}$ and $z_\odot \simeq 0$, gives the

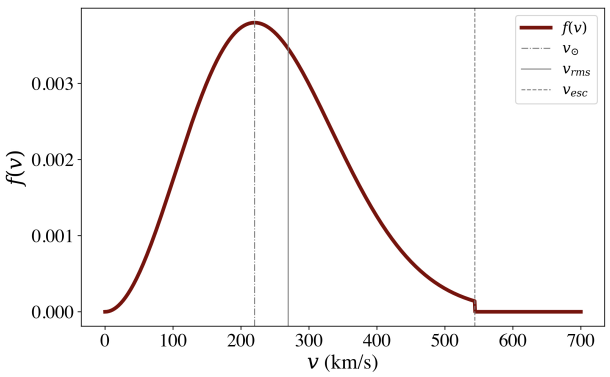


Figure 7: Maxwellian velocity profile for dark matter located 8 kpc from the center of the Milky Way. $v_\odot$ is azimuthal velocity of the Sun in the galactic plane and $v_{\rm rms}$ is the root mean square velocity for the Maxwellian distribution. The distribution drops to zero at the galactic escape velocity $v_{\rm esc} \approx 544 {\rm km/s}$.

local DM density:

$$\rho^\odot_{\rm DM} = 0.0155\, M_\odot\, {\rm pc}^{-3} = 0.589\, {\rm GeV/cm}^3. \quad (34)$$

We will use this value throughout our analysis.

The local PBH differential number density will therefore be given by

$$\frac{dn}{dM} = f_{\rm PBH}\, \rho^\odot_{\rm DM} \frac{1}{M} \psi(M, t_0), \quad (35)$$

where $\psi(M, t_0)$ is the present-day mass function computed according to Section II B 3.

2. *Dark Matter Velocity Profile*

We treat our local region of the DM halo as a volume of isotropically distributed, non-interacting PBHs with a fixed number density given by the integral of Eq. (35). We neglect any potential effects due to PBH interactions, clustering, or binaries [14].

This population of PBHs will obey a Maxwellian velocity distribution [116, 117]:

$$f(v) = \frac{4 f_0}{\sqrt{\pi}} \left(\frac{3}{2}\right)^{3/2} \frac{v^2}{v^3_{\rm rms}} \exp\left[-\frac{3}{2}\frac{v^2}{v^2_{\rm rms}}\right]; \;\; v < v_{\rm esc}. \quad (36)$$

We assume that the Sun is located at $r_\odot = 8.0 \pm 0.5$ kpc, which corresponds to $v_\odot = 220 \pm 20$ km/s [116]. The velocity dispersion is related to the Sun's azimuthal velocity in the galactic plane via $v_{\rm rms} = \sqrt{3/2}\, v_\odot \approx 270$ km/s [117]. Truncating Eq. (36) at the galactic escape velocity $v_{\rm esc} = 544$ km/s sets the normalization constant $f_0 = 1.00684$. This DM velocity profile is plotted in Figure 7.

More complicated models of local DM velocity distributions include modified Maxwellians [118], Eddington inversion methods [119], and results from numerical simulations. (See Ref. [117] for a review.) Furthermore, observational measurements hint at possible sources of local DM density and velocity anisotropies due to astrophysical phenomena like the Nyx stellar stream [120, 121]. This object is a high-eccentricity, prograde stellar stream within the Milky Way thin disk which may be the remnant of an ancient collision between a dwarf galaxy and the Milky Way [120]. If Nyx is the result of a dwarf galaxy collision, it would contribute to the local dark matter substructure and affect direct detection experiments [122]. The impact on PBH transit rates caused by such modifications to the local DM velocity profile is beyond the scope of this paper.

In the following analysis we assume PBHs obey Eq. (36) and that the out-of-the-galactic-plane (v_z) and radial (v_r) velocity components are negligible in comparison to the azimuthal velocity v_ϕ. Because the relative velocity between the Earth and the Sun is $\sim 0.1 v_{\rm rms}$, we also assume that the contribution from Earth's orbit around the Sun to $f(v)$ is negligible with respect to $v_{\rm rms}$. This amounts to a purely azimuthal PBH "wind" with $v_\phi \approx \bar{v} = 246$ km/s flowing past the Earth, analogous to the "WIMP wind" discussed in association with WIMP direct detection experiments.

D. Detector Geometry

In this section we discuss the technical considerations relevant to measuring Hawking radiation from low-mass PBHs transiting past Earth with a detector stationed in low-Earth orbit (LEO). Figure 2 shows secondary emission spectra for select PBHs in the positron-producing mass range, $M_* \leq M \leq 5\times10^{17}$g. Because the particles emitted during these close encounters would only propagate over length scales of $\mathcal{O}(1\,{\rm AU})$ rather than over kiloparsecs, we can neglect modifications due to energy loss, scattering, and diffusion effects typically relevant for computing cosmic ray spectra. However, the shape and energy range of the measured signal will be modified by the geomagnetic field and the specific detector geometry.

The Alpha Magnetic Spectrometer (AMS) is a candidate experiment to detect Hawking radiation from transiting PBHs, with over 10 years of high-precision time-series positron flux data [123]. Other detectors with potentially useful datasets include FERMI-Lat, which could also study coincident time-dependent γ-ray and $e^\pm$ signatures, PAMELA, and Voyager-1 (which would not be subject to the geomagnetic field constraints discussed in following subsections).

We focus on positron signatures in this article because PBHs emit e^+ and e^- at equal rates but positrons have a significantly lower astrophysical background. Section III B 2 address the complexities of the positron background and the effects of solar modulation on our signature. Time-series analysis of e^+ fluxes is uniquely possible with AMS data because of the high charge separation resolution made possible by the AMS 0.15 T permanent magnet. The electron charge confusion fraction is below one in 10^4 for energies below 30 GeV [16]. Other charged lepton Hawking radiation constraints, such as those placed by Voyager-1 data [59], are computed with $(e^- + e^+)$ fluxes.

1. Geomagnetic Field

Measuring charged cosmic rays with a detector in LEO requires an understanding of the magnetosphere, the volume around Earth dominated by its magnetic field. Earth's magnetic field at radius r, latitude θ, and longitude λ can be described by the spherical harmonic expansion of a scalar potential Ψ:

$$\Psi(r,\theta,\lambda) = a\sum_{l=1}^{\infty}\sum_{m=0}^{l}\left(\frac{a}{r}\right)^{l+1}\Big[C_l^m\cos(m\lambda) + S_l^m\sin(m\lambda)\Big]P_l^m(\cos\theta), \tag{37}$$

which satisfies $\vec{B} = -\nabla\Psi$ and $\nabla^2\Psi = 0$ [124, 125]. In Eq. (37), a is a reference radius and C_l^m and S_l^m are often referred to as *Gauss coefficients* which can be fit to geomagnetic field data using an appropriate reference radius [126].

The geomagnetic field can be approximated by the $l = 1$ dipole term of Eq. (37) with magnetic moment $7.7\times10^{22}\,\mathrm{Am}^2$ [125]. The magnetic moment is not static spatially or temporally and has fluctuated and reversed over the course of Earth's history. Recent measurements show the dipole moment has been decreasing since at least the year 1600 [127]. Archeomagnetic and paleomagnetic data from core samples, thermoremnant magnetization, and archaeological samples show complex variation of the dipole moment over large time-scales [127, 128], and evidence that the geomagnetic field reverses over uncorrelated intervals of tens of thousands to millions of years in a statistically random process [129, 130]. The dipole axis is not parallel to the Earth's rotation axis, and the magnetic north dipole is currently located near 86.5^o latitude [125]. The locations of the magnetic poles drift with time, and are projected by the most recent International Geomagnetic Reference Field report to travel at an average rate of 40km/yr from 2020-2025 [125]. Since 1900, the magnetic North pole has traveled northward by approximately 15^o latitude [125].

Assuming a dipole field geometry, the Stoermer approximation can be used to estimate the *geomagnetic cutoff* rigidity R_c [131]:

$$R_c = \frac{\mathcal{M}\cos^4\theta}{r^2\left[1+\sqrt{1-\sin\epsilon\sin\xi\cos^3\theta}\right]^2}. \tag{38}$$

This cutoff is the minimum *rigidity* (momentum per unit charge) necessary for a particle to reach a point in the magnetosphere from infinity, and it is generally a function of particle path, location, and geomagnetic field [132]. R_c, with units of MV, is a function of radius r in cm, magnetic latitude θ, azimuthal angle ξ, zenith angle ϵ, and magnetic moment $\mathcal{M}$ in $\mathrm{G}\cdot\mathrm{cm}^3$, all defined in Ref. [133]. The geomagnetic cutoff rigidity ranges from about 15 GV at the equator to 0 GV at the magnetic poles, where the tangential component of the field vanishes. Sub-GeV charged cosmic rays can therefore only be detected by an experiment in LEO when its orbit takes it near the magnetic poles—where charged particles can penetrate to lower altitudes. This reduces both the measured positron signal and background and significantly reduces the proton background at low energies for an experiment in LEO. We include the effect of the geomagnetic cutoff in our simulations of time-dependent positron signals from PBH transits measured by AMS in section III B.

2. AMS Detector

AMS is a precision particle physics experiment aboard the International Space Station (ISS) equipped with a 0.15 T permanent magnet and six detector subsystems designed to measure the charge q, momentum p, velocity $\beta \equiv v/c$, and rigidity $R \equiv p/q$ of fundamental particles and nuclei [16]. The detector stack includes 9 silicon tracker layers, a Transition Radiation Detector (TRD), upper- and lower- Time of Flight (TOF) counters, an Anti-Coincidence Counter (ACC) surrounding the magnet bore, a Ring Imaging Cherenkov (RICH) detector, and an Electromagnetic Calorimeter (ECAL). AMS has been operating since 2011 and to date has published data from 3.4×10^6 positrons with energies between 500 MeV and 1 TeV [123, 134].

AMS is subject to the ISS orbital trajectory in LEO with an inclination of 51.6^o and a period of 90 minutes. As discussed in the previous subsection, because the geomagnetic north dipole has moved to such a high latitude over the past decades, experiments like AMS—even with its high orbital inclination—are quite constrained by the geomagnetic cutoff. AMS is only able to measure low rigidity (sub-GV) particles at the most extreme northern and southern latitudes of its orbit. As a result, observation time for 1 GV positrons is only on the order of 1000 seconds per day [123].

Other constraints on the energy range and precision of low-energy positron measurements with AMS come from the AMS Level-1 trigger, particle track curvature, detector resolution, and background rejection efficiency. The Level-1 trigger for electrons and positrons requires a coincidence of hits on all 4 TOF layers and a minimum ECAL energy deposition [16]. Considering that the upper and lower TOF counters (with two layers each) are separated by 1.25 m [135], and accounting for the thickness of the RICH (0.47 m) [136] and the ECAL (0.167 m) [16], the total distance from the top TOF layer to the bottom of the ECAL is $\sim 2\,\mathrm{m}$. Therefore, an estimate for the minimum radius of curvature such that an incident positron can hit both TOF counters and the ECAL is about 1 m, which translates to a minimum detectable positron energy of ∼50 MeV.

There is a reported drop in the AMS Level-1 trigger efficiency starting at around 3 GeV and reaching an efficiency of $\sim 80\%$ for 500 MeV electrons [16]. Furthermore, ECAL energy resolution rises above the 10% level for $e^{\pm}$ below 1 GeV and proton rejection rates from the TRD and ECAL drop by several orders of magnitude for sub-GeV positrons [16]. The combination of these detector properties and the geomagnetic cutoff has led the AMS collaboration to only publish on positrons with energy $Q \geq Q_{\min} = 500$ MeV, for which statistics are relatively high.

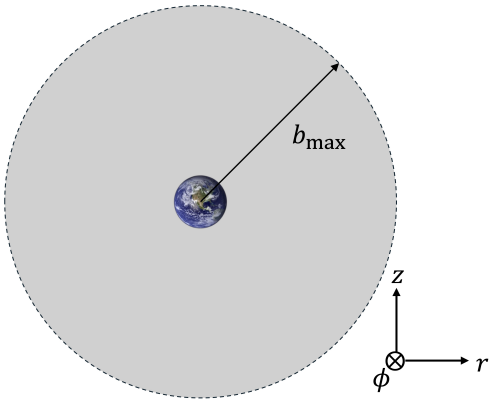


Figure 8: Schematic of the transit geometry discussed in Section III A. PBHs traveling in the $\hat{\phi}$ direction, parallel to the galactic plane, will transit past Earth within some impact parameter $b_{\rm max}$ at a rate given by Eq. (40).

In Sec. III we study the feasibility of using published time-series e^+ flux data from AMS to detect time-dependent positron signatures from nearby PBH transits. We further discuss applying this analysis technique to potential future positron datasets. The lower the positron energy that the data includes, the larger the space of PBH mass function models that we can probe.

III. RESULTS

A. PBH Transit Rates

We estimate the number of PBHs that will transit past the Earth per year with impact parameter b. We let $f_{\rm PBH} = 1$ because we aim to generate new constraints independent of existing evaporation constraints. A schematic of the transit geometry is depicted in Figure 8. We assume that PBHs with masses distributed according to a present-day mass function $\psi(M, t_0)$ are traveling parallel to the galactic plane with azimuthal velocity v_ϕ distributed according to Eq. (36) and that $v_\phi \gg v_r, v_z$.

The differential transit rate for PBHs of mass M, velocity v, and impact parameter b is:

$$\frac{d^3\Phi_{\rm transit}}{dM dv db} = \frac{dn}{dM}(v f(v))(2\pi b). \tag{39}$$

Here we have assumed that the mass and velocity distributions are locally isotropic. We may then estimate the number of PBHs with masses up to some maximum mass $M_{\rm max}(t_0)$ today that should transit past the Earth per unit time with impact parameter $b \leq b_{\rm max}$. We average over the velocity distribution $f(v)$, integrate over the mass range $0 \leq M(t_0) \leq M_{\rm max}(t_0)$, and integrate up to $b_{\rm max}$, which might be mass-dependent:

$$\bar{\Phi}_{\rm transit}(M_{\rm max}, b_{\rm max}) = \rho^{\odot}_{\rm DM} \int_0^{M_{\rm max}} dM\, \frac{1}{M}\psi(M, t_0) \times \int_0^{v_{\rm esc}} dv\, v f(v) \int_0^{b_{\rm max}(M)} db\, 2\pi b, \tag{40}$$

where the over-bar indicates averaging over the PBH velocity distribution and $\rho^{\odot}_{\rm DM}$ is the local dark matter mass density given by Eq. (34). Here we have used the definition of dn/dM from Eq. (35) with $f_{\rm PBH} = 1$.

As noted above, only PBHs with present-day mass $M(t_0) \leq 5 \times 10^{17}\,{\rm g}$ will emit electrons and positrons. Hence to study the number of PBH transits that could yield detectable positrons today, we consider the quantity

$$\bar{\Phi}_{e^\pm}(b_{\rm max}) \equiv \bar{\Phi}_{\rm transit}(5 \times 10^{17}\,{\rm g}, b_{\rm max}). \tag{41}$$

Given how modest the mass-loss due to Hawking evaporation is over the current age of the universe for $M_i = 5 \times 10^{17}\,{\rm g} \gg M_* = 5.34 \times 10^{14}\,{\rm g}$, we incur an error of only $(M(t_0, M_i) - M_i)/M_i = -3.6 \times 10^{-10}$ for $M_i = 5 \times 10^{17}\,{\rm g}$, per Eq. (19). Hence we may use the positron-emitting mass $M(t_0) \simeq M_i = 5 \times 10^{17}\,{\rm g}$ when evaluating $\bar{\Phi}_{e^\pm}(b_{\rm max})$.

The PBH transit rate $\bar{\Phi}_{e^\pm}(b_{\rm max})$ is model-dependent and therefore a function of either the GCC model parameters μ, α, and β or the LN model parameters μ, σ. Figure 9 shows the yearly transit rate $\bar{\Phi}_{e^\pm}$ for $b_{\rm max} = 1\,{\rm AU}$ and $t = t_0$ as a function of the respective model parameters for both GCC and LN mass functions. For both models, we expect at least one transit per decade for $M_i \lesssim 10^{18}\,{\rm g}$. It is encouraging that a cosmic ray experiment with a decade of data could potentially probe such a large space of models via a careful time-series analysis.

Given that both the GCC and LN parameter spaces admit such high transit rates for $f_{\rm PBH} = 1$, one may wonder whether PBHs colliding with the Earth, Sun, or other Solar System bodies would provide better constraints on the dark matter fraction of low-mass PBHs than Hawking radiation signatures. Stellar capture of PBHs was first posited by Hawking [2]. Recent work estimates stellar capture rates [137–144] and analyzes the evolution of "Hawking stars" with captured black holes at their centers [145–147]. Potential signatures of Hawking stars would be unique solar seismological signals or disappearing stars [144, 146], or weak gravitational-wave signals from bound-PBH orbits within its host star [148]. Stellar capture rates are predicted to be quite low, however, and none of these signatures have yet been observed. Refs. [149, 150] discuss the morphology of craters from PBH impacts on rocky bodies and suggest that a study of lunar craters may provide PBH dark matter constraints. We estimate that, for a LN mass function with $\mu \in [M_*, 5 \times 10^{17}\,{\rm g}]$ and $\sigma \in [0.1, 2]$ (the parameter space shown in Fig. 9), between about 1 and 4000 PBHs would have impacted the Earth over its 4.54 Gyr existence. Given that impact rates are so low and because the Earth is tectonically active, this is not a likely detection strategy.

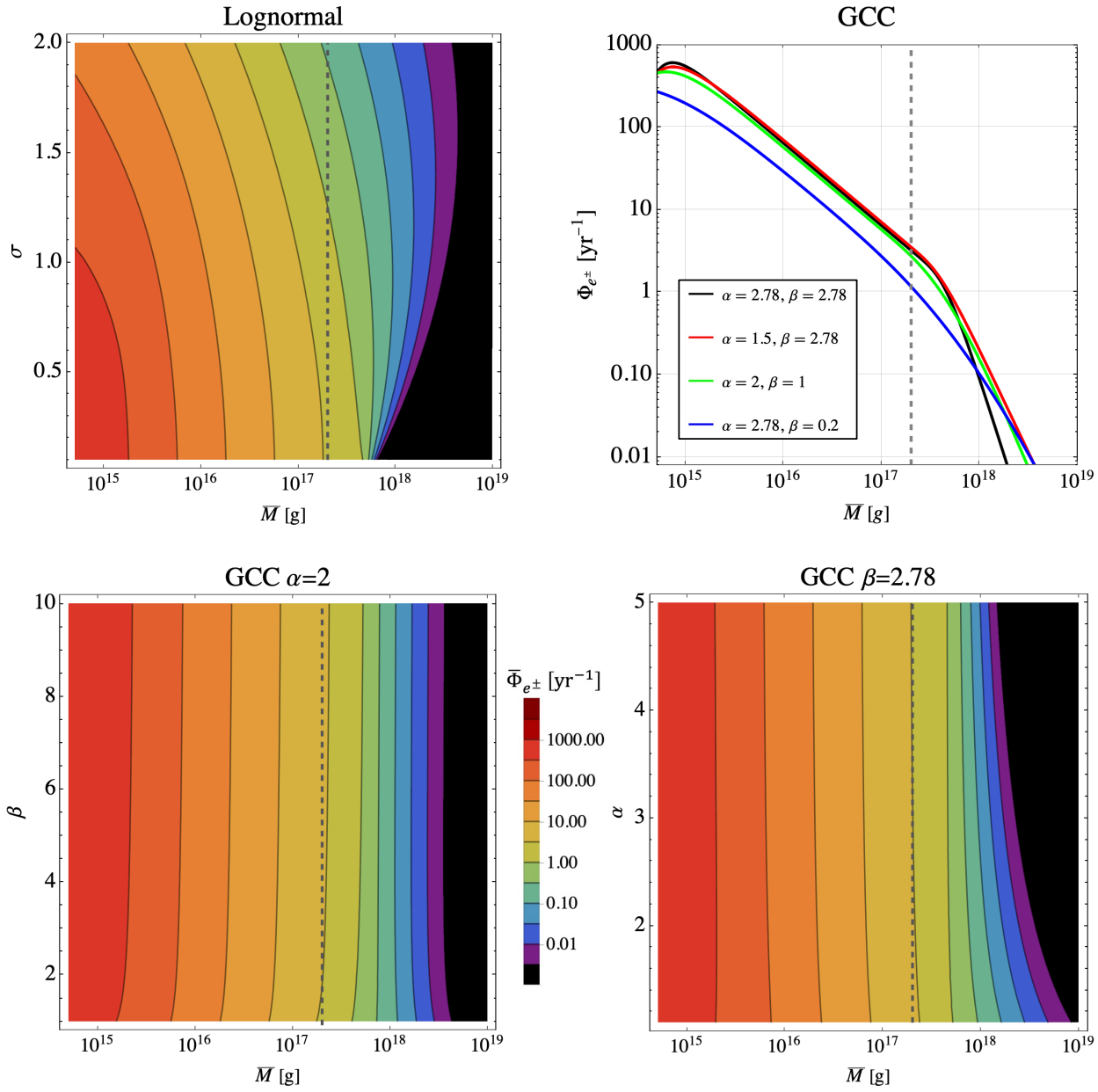


Figure 9: Number of expected positron-producing PBHs that pass within 1 AU of Earth per year. Here we plot the yearly transit rate $\bar{\Phi}_{e^\pm}$ according to Eq. (41) with $b_{\rm max} = 1\,{\rm AU}$, $t = t_0$, and $f_{\rm PBH} = 1$, as a function of the mass $\bar{M}_i$ at the peak of the formation-time PBH mass function, given in Eqs. (11) and (13) for the GCC and LN functions, respectively. Rates for the LN mass function range from $0.005 - 1065\ {\rm yr}^{-1}$ for $0.1 \leq \sigma \leq 2.0$. The GCC PBH transit rate (top right) is plotted as a function of $\bar{M}_i$ and shown for three sets of parameters $\{\alpha, \beta\}$. Contour plots of the GCC PBH transit rate with α constant (bottom, left) and β constant (bottom, right) indicate that the transit rate is only weakly sensitive to α and β for $\bar{M}_i > M_*$. For both models, if $\bar{M}_i$ falls in the positron-producing mass range, $M_* \leq \bar{M}_i \leq 5 \times 10^{17}$g, the expected transit rates exceed $1\,{\rm yr}^{-1}$, which implies that a decade of precision time-series data could probe large regions of parameter space. Vertical dashed lines at $\bar{M}_i = 2 \times 10^{17}\,{\rm g}$ indicate the mass where current evaporation constraints on extended mass functions stop and $f_{\rm PBH} = 1$ is viable [15, 62]. Note that detectable positron signals could arise even for $\bar{M}_i > 5 \times 10^{17}\,{\rm g}$ because we have incorporated realistic, extended mass functions and evolved them from the time of PBH formation to today; hence a subpopulation of PBHs with $M(t_0) \leq 5 \times 10^{17}\,{\rm g}$, capable of emitting positrons today, would emerge from the small-mass tail of the underlying PBH mass function.

Searching for evidence of PBH transits through the significantly larger volume of the inner Solar System, however, allows high enough transit rates that we may see PBH candidates within the approximately decade-long lifetimes of existing cosmic ray experiments—even for models peaked in the unconstrained asteroid-mass range where number densities are lower. Note that other recent analyses that study gravitational perturbations from PBH flybys also find comparable transit rates to those calculated in this study, but do not use time-evolved PBH mass functions [65, 66].

B. Time-Dependent PBH Signature

The goal of this section is to develop an analysis technique to extract a PBH transit signal from time-series cosmic ray flux data, and to estimate an upper bound on detection efficiency for a given detector geometry when transit parameters M, v and b are known. We specifically perform numerical studies to determine how reliably the AMS experiment could detect time-dependent positron excesses corresponding to PBH transits with mass M and impact parameter b.

We first develop a Monte Carlo simulation to model the measured Hawking emission signal from a transiting PBH within a noisy positron background. Section III B 1 derives analytically the estimated time-dependent positron count-rate measured by the AMS detector in orbit around the Earth during a PBH transit. In Sec. III B 2 we construct our positron background using mean fluxes and temporal fluctuation amplitudes sampled from AMS data [123, 134]. Then in Sec. III B 3 we discuss low-SNR peak detection with matched filters. In Sec. III B 4 we develop a measure of "detectability" for a transit with parameters M and b and compute the *maximum detectable impact parameter*, $b_{\rm max}(M)$ for a PBH of mass M. Section III B 5 utilizes our simulation results to update the plots in Fig. 9 by computing the number of *detectable* positron-producing PBH transits per year as a function of model parameters for simulated positron datasets from each of three detector configurations.

The three detector configurations, with parameter values listed in Table I, are: (1) AMS aboard the ISS in low-Earth orbit, (2) AMS in geosynchronous orbit, and (3) a hypothetical detector located at a Lagrange point outside the geomagnetic field. For configuration (2), we posit that a future positron dataset extending down to approximately $Q_{\rm min} = 50\,{\rm MeV}$ could be collected by an instrument similar to AMS (or AMS itself) in geosynchronous orbit rather than from LEO. With a height $h \approx 36,000\,{\rm km}$, an instrument in geosynchronous orbit would see a maximum Stoermer cutoff rigidity at equatorial latitudes of $R_c \approx 48\,{\rm MeV}$ [151–154]. Furthermore, as discussed in Sec. II D 2, we estimate that based on AMS detector geometry, the minimum positron energy that would correspond to a detectable radius of curvature and an ECAL hit would be $\mathcal{O}(50\,{\rm MeV})$. Similarly, for configuration (3) we consider a hypothetical detector of similar resolution and acceptance to AMS, but located even farther outside the Earth's magnetosphere—such as at a Lagrange point. Such a detector, with instrument modifications like a weaker magnetic field strength, could be sensitive to positrons with energies $Q \geq 5\,{\rm MeV}$ and could probe a much wider space of realistic PBH mass functions. We identify regions of model parameter space that could be explored with each dataset.

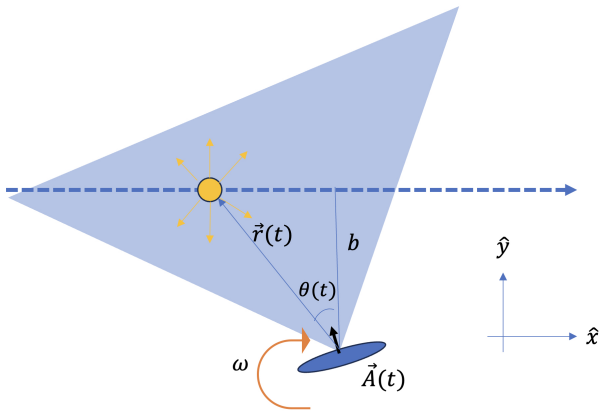


Figure 10: Geometry for simulating the time-dependent e^+ signal from a PBH transit measured by a detector in orbit about the Earth. The blue field of view cone rotates with the detector area $\vec{A}(t)$ about a fixed point at frequency $\omega = 2\pi/\tau$. We approximate the orbit as rotation about a fixed point because $b \gg R_\oplus + h$. The PBH (yellow circle) transits past on a linear trajectory with velocity $\bar{v} = 246\,{\rm km/s}$ while emitting positrons at a rate $\dot{N}(M)$ given by Eq. (43).

	AMS in LEO	Geosynch.	Lagrange Pt.
$Q_{\rm min}$ [MeV]	500	50	5
τ	90 minutes	1 day	No rotation
a [m^{2}sr]	0.055	0.165	0.165
$\theta_{\rm FOV}$ [rad]	0.168	0.292	0.292
$\tau_{\rm obs}(Q)$	[0,1.0]	1.0	1.0

Table I: The three detector configurations simulated in this study, corresponding to AMS in low-Earth orbit, AMS in geosynchronous orbit, and a hypothetical detector located at a Lagrange point well outside the geomagnetic field. The parameter $\tau_{\rm obs}(Q)$ encodes the effects of the geomagnetic field via imposing latitude-dependent cutoff rigidities. For AMS in LEO, $\tau_{\rm obs}(Q)$ is interpolated form reported values and spans the range $[0, 1.0]$ for particle energies between 100 MeV and 50 MeV.

1. *Simulated PBH Signals*

We first compute the time-dependent positron signal generated by a transiting PBH and measured by an ideal detector in orbit around the Earth. The orbit, which approximates that of the ISS, is parameterized by a height $h = 450$ km, a period $\tau = 90$ min, and an inclination of $\pm 51.6^o$ latitude. Our ideal detector, which measures positrons with 100% ef-

ficiency, has a field of view (FOV) angle $\theta_{\rm FOV}$, an oriented area $\vec{A}(t)$, an energy-dependent acceptance $a(Q)$, and a minimum detectable positron energy $Q_{\rm min}$. This $Q_{\rm min}$ parameter is determined in practice by the detector geometry, efficiency, trigger, and orbit relative to the geomagnetic field. For AMS, we take $Q_{\rm min} = 500\,{\rm MeV}$, as discussed in Section II D 2.

We use a 2D geometry. The PBH trajectory past Earth is parameterized by $\vec{r}(t) = \bar{v}t\hat{x} + b\hat{y}$, with average velocity $\bar{v} = 246\,{\rm km/s}$ and impact parameter $b \gg R_\oplus + h$. These parameters are listed in Table II and a schematic of the transit geometry is shown in Fig. 10. The two independent parameters of this model are M and b; velocity $v = \bar{v} \equiv 246\,{\rm km/s}$ is held constant. Parameters that depend on the detector configuration include: orbital period τ, acceptance $a(Q)$, FOV angle $\theta_{\rm FOV}$, and minimum detectable positron energy $Q_{\rm min}$.

Given a PBH mass M, we numerically compute the secondary positron Hawking emission spectrum, $d^2N^{(2)}_{e^+}/dtdQ$, using `BlackHawk v2.2`. Figs. 1–2 show secondary positron spectra for several PBH masses in the positron-producing range.

To determine the observable positron flux, we numerically integrate the secondary emission spectrum weighted by the energy-dependent observation time fraction $\tau_{\rm obs}(Q)$ between $Q_{\rm min}$ and some $Q_{\rm max}$. The observation time fraction is a dimensionless parameter that varies with particle energy Q which represents the fraction of time that the detector is at a magnetic latitude with cutoff rigidity $R_c \leq Q$. We compute $\tau_{\rm obs}(Q)$ by interpolating the daily AMS energy-dependent observation times from Ref. [123], assuming that $\tau_{\rm obs} = 0$ for 100 MeV, and dividing by the number of seconds in a day. Note that, in this context, "observable" refers to energies $Q \geq Q_{\rm min}$, which imposes that the emitted positions have an energy greater than the detector's minimum threshold.

The upper bound cut at $Q_{\rm max}$ is more arbitrary, and should be chosen to capture the peak of the Hawking emission spectrum while avoiding background so as to maximize the signal-to-noise ratio (SNR). We take a simple approach here and define $Q_{\rm max}(M)$ to depend on the PBH mass such that it is larger than $Q_{\rm min}$ and satisfies:

$$\int_0^{Q_{\rm max}} \frac{d^2N^{(2)}}{dtdQ}dQ \Big/ \int_0^{\infty} \frac{d^2N^{(2)}}{dtdQ}dQ \geq 0.99. \tag{42}$$

This method of defining $Q_{\rm max}$ captures the greatest available signal but is not optimized to reduce noise and thereby maximize SNR. Improved methods would include making cuts to avoid the noisiest energy range around $\sim 1\,{\rm GeV}$ and/or performing this analysis separately on many energy bins rather than integrating up the entire signal with respect to energy.

The total emission rate of observable positrons emitted by the transiting PBH of mass M is thus:

$$\dot{N}(M) = \int_{Q_{\rm min}}^{Q_{\rm max}} dQ\, \tau_{\rm obs}(Q) \frac{d^2N^{(2)}_{e^+}}{dtdQ}(M,Q). \tag{43}$$

The weighting by $\tau_{\rm obs}$ in Eq. (43) approximately accounts for the changing geomagnetic cutoff due to variations in latitude during the orbits. Estimating observation time for positrons in a given energy bin is quite complicated for a real detector like AMS, which not only orbits the Earth and traverses $\pm 51.6^o$ of latitude, but is subject to various ISS maneuvers which change its pointing dynamically with time. Furthermore, the geomagnetic field is dynamic and has many features not captured by Stoermer's dipole approximation, such as the South-Atlantic Anomaly, where field intensity drops to about 1/3 of the typical intensity and particle fluxes increase dramatically [155]. A more accurate determination of observation time as a function of positron energy would require ISS trajectory and altitude data, AMS orientation data (which is collected by an onboard GPS), and the International Geomagnetic Reference Field—a precise model of the time-varying geomagnetic field [125]. This is beyond the scope of this analysis.

We assume ballistic transport to propagate the emitted positrons to Earth and ignore the diffusive transport effects characteristic of charged particle propagation. This is a good approximation in our regime of interest because the parallel and perpendicular mean free paths for $e^\pm$ diffusion exceed 10^{-3} AU for all particle energies $Q \geq 5\,{\rm MeV}$ at a distance of 1 AU in the heliospheric magnetic field [156–158]. The mean free paths set the typical length scale that a charged particle will travel before scattering off a magnetic field inhomogeneity.

We define the angle between the PBH at point $\vec{r}(t)$ and the detector area vector $\vec{A}(t)$ as:

$$\theta(t) \equiv \cos^{-1}\left(\frac{\vec{r}(t)\cdot\vec{A}(t)}{|r(t)||A(t)|}\right), \tag{44}$$

which is labeled in Fig. 10.

We can then define the time-dependent positron signal count rate measured by our ideal orbiting detector as $\zeta_{e^+}(t)$, with dimensions s^{-1}:

$$\begin{aligned}\zeta_{e^+}(t|M,b) =& \frac{A\dot{N}(M)}{4\pi(\bar{v}^2t^2+b^2)^{3/2}}\Theta(\theta_{\rm FOV}-\theta(t)) \\ &\times\left[vt\sin\left(\frac{2\pi}{\tau}t\right) + b\cos\left(\frac{2\pi}{\tau}t\right)\right].\end{aligned} \tag{45}$$

Note that this expression for $\zeta_{e^+}(t)$ quantifies the incident positron count rate in the energy range from $Q_{\rm min}$ to $Q_{\rm max}$ as measured by an orbiting detector; for a stationary detector, we only need the terms in the first line of Eq. (45). The integrated Hawking emission rate $\dot{N}(M)$ is defined in Eq. (43). The Heaviside theta function $\Theta(\theta_{\rm FOV} - \theta(t))$ imposes that the signal vanishes where $\theta(t) > \theta_{\rm FOV}$, corresponding to intervals when the PBH is outside the FOV cone of the detector. Note that we use the assumption $b \gg R_\oplus + h$ to approximate the orbit of the detector about the Earth as rotation of the detector about a fixed point with period τ. See Fig. 11 for plots of count-rate $\zeta_{e^+}(t)$ for the AMS experiment for various PBH masses and impact parameters.

The FOV angle $\theta_{\rm FOV}$ that appears in Eq. (45) can be computed from the detector acceptance and a few reasonable assumptions. Detector acceptance is the quantity that allows one

Symbol	Definition	Units
M	PBH mass	g
b	Impact parameter	AU
$\bar{v}$	Average PBH velocity	km/s
t	Time since closest approach	s
$\vec{r}(t)$	PBH position	AU
Q	Positron energy	GeV
h	Orbit altitude	km
τ	Orbit period	minutes
$\theta_{\rm FOV}$	Detector field of view angle	radians
$\vec{A}(t)$	Oriented detector area	m^2
$a(Q)$	Detector acceptance for $e^{\pm}$ with energy Q	$\mathrm{m}^2\mathrm{sr}$
$Q_{\rm min}$	Detector minimum detectable $e^{\pm}$ energy	GeV
$\tau_{\rm obs}(Q)$	Observation time fraction for $e^{\pm}$ with energy Q	
$\zeta_{e^+}(t)$	Measured PBH positron count-rate signal	s^{-1}
$\mathcal{A}$	Amplitide of measured PBH positron rate count-rate signal	
μ	lognormal model location parameter	g
σ	lognormal model width parameter	
α	GCC low-mass tail model parameter	
β	GCC high-mass tail model parameter	
$\bar{\Phi}_{e^{\pm}}$	e^+-producing PBH transit rate past Earth	yr^{-1}
$b_{\rm max}(M)$	Maximum impact parameter for detectable transit	AU
ϕ_i	Measured AMS $e^{\pm}$ flux for energy bin i	$\mathrm{m}^{-2}\mathrm{s}^{-1}\mathrm{sr}^{-1}\mathrm{GeV}^{-1}$

Table II: Symbol definitions and values for PBH transit simulation parameters and relevant variables. Only PBH mass M and transit impact parameter b are independent simulation parameters. The detector orbit and geometry parameters vary depending on which detector configuration is being considered, and are tabulated in Table I.

to translate between a particle flux—a physical quantity independent of the measuring instrument—and the particle count rate measured by a specific instrument over a given time interval. We can define an energy-dependent acceptance as the product of the detector efficiency ϵ, which includes contributions from trigger and selection efficiencies, and the detector geometric acceptance $a_{\rm geo}$:

$$a(E) = \epsilon(E)\, a_{\rm geo}(E). \tag{46}$$

The geometric acceptance, with dimensions $\mathrm{m}^2\mathrm{sr}$ is effectively the product of the detector's sensitive area A and the solid angle Ω swept out by its field of view. Assuming 100% efficiency for our idealized detector ($\epsilon = 1$), we can thus relate known quantities a and A to $\theta_{\rm FOV}$ via the geometric acceptance:

$$a = A\Omega = A \int_0^{2\pi} d\phi \int_0^{\theta_{\rm FOV}} d\theta\, \sin\theta. \tag{47}$$

We take the detector sensitive area to be the size of one of the nine silicon tracker layers, which are not uniform in area. A representative area can be approximated by dividing the total reported sensitive detector area $6.75\,\mathrm{m}^2$ by 9, which yields $A = 6.75/9 = 0.75\,\mathrm{m}^2$ [159]. We use the more conservative area value $A = 0.62\,\mathrm{m}^2$.

For the unmodified AMS detector configuration, we use the reported geometric acceptance $a_{\rm geo}^{\rm AMS} = 0.055\,\mathrm{m}^2\mathrm{sr}$ [160]. For the two hypothetical detector scenarios, we note that the planned Layer-0 AMS upgrade predicts a 300% increase in acceptance by the inclusion of two additional large-area silicon tracker layers to the top of the instrument stack [161]. We thus optimistically take $a_{\rm geo} = 3a_{\rm geo}^{\rm AMS} = 0.165$ for these cases. The derived values for $\theta_{\rm FOV}$ are thus $\theta_{\rm FOV} = 0.153\,\mathrm{rad}$ for AMS and $\theta_{\rm FOV} = 0.265\,\mathrm{rad}$ for the hypothetical large-acceptance configurations.

Figure 12 shows in green the positron signal count measured by our ideal AMS detector with no background for $M = 10^{14}$ g and $b = 0.5\,\mathrm{AU}$ binned over intervals of 0.25 days.

The signal counts are binned over intervals of 0.25 days, thus averaging over 4 orbital cycles for each bin. Each time-dependent transit signal is characterized by its amplitude, time of closest approach, and full width at half maximum (FWHM), which can be used as a measure of the effective "duration" of the transit. For the Lorentzian envelope in Eq. (45), the FWHM is determined by the PBH velocity and impact parameter:

$$\mathrm{FWHM} = \frac{2b}{v}. \tag{48}$$

Figure 12 compares the binned positron count signals measured by a stationary and rotating AMS detector. At time-of-closest-approach, the stationary signal is about 10 times larger, but its duration is quite short (1 day) due to the detector's narrow FOV, compared with the 7 day FWHM of the signal seen by the rotating detector. The resulting integrated

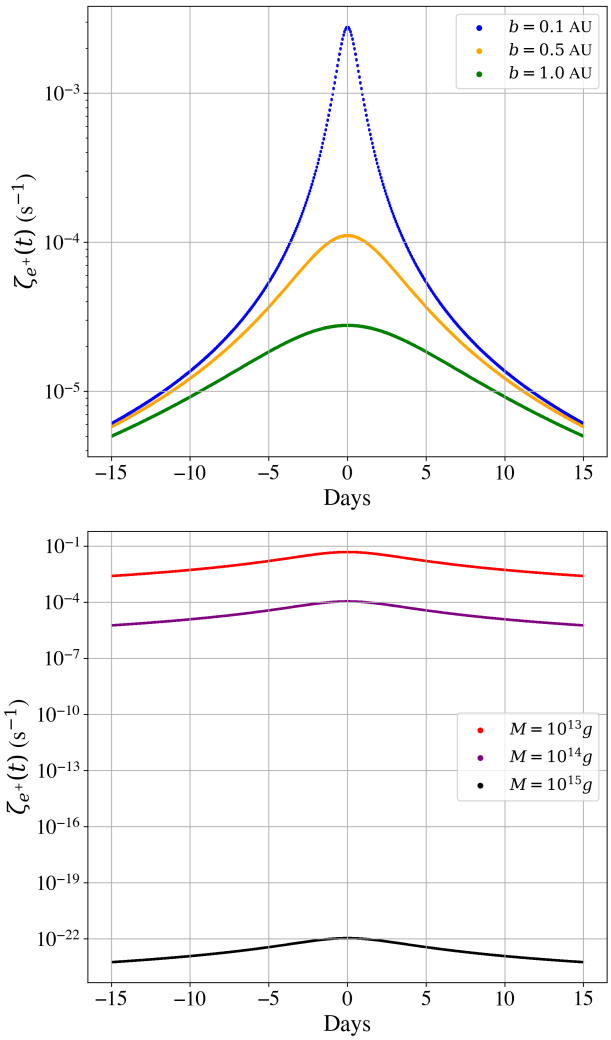


Figure 11: Time-dependent positron count-rates $\zeta(t|M, b)$ for PBHs transiting past an ideal detector in orbit around Earth. These count-rates are calculated from Eq. (45). Note that the curves appear to be dotted lines because they are highly oscillatory functions with a Lorentzian envelope. The oscillations have period $\tau \ll$ FWHM determined by the detector orbital frequency, and the count-rate signal is zero when the PBH is outside the detector FOV, causing the signal to vanish periodically. Time $t = 0$ corresponds to the point of closest approach to Earth. The signal for a 10^{15} g PBH (green curve, bottom panel) is negligible because AMS is only sensitive to positrons with energies $Q \geq 500\,\mathrm{MeV}$ and the Hawking emission spectrum for 10^{15} g PBHs, as shown in Fig. 1, cuts off around $100\,\mathrm{MeV}$.

positron counts differ by only a factor of 2 instead of 10, as discussed in the caption. Thus, implementing a stationary detector for the third detector configuration gives an SNR boost by a factor of ~ 10, but PBH detection is limited by the time-resolution of the binned data.

To determine whether these time-dependent positron fluctuations are detectable with AMS, we must accurately simulate the time-varying positron background. Using a matched filter and proper binning in time, we find that we can detect low-mass PBH transits with SNR $\lesssim 1$.

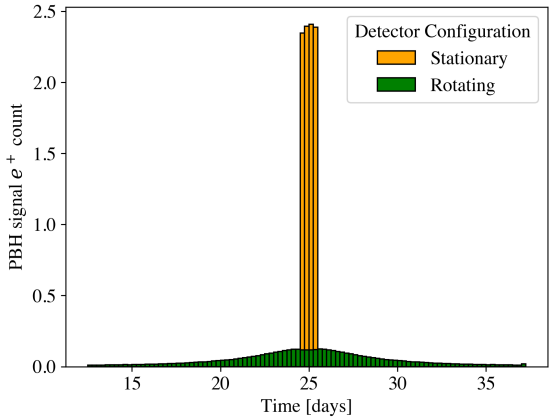


Figure 12: Positron counts binned every 0.25 days for the measured signal generated by a 10^{14} g PBH transiting past Earth with an impact parameter of $b = 0.5\,\mathrm{AU}$. The signal observed by a stationary detector (yellow) is compared with the signal observed by a detector rotating with a period of 90 minutes (green). The integrated positron counts observed throughout the entire transit duration are 9.5 counts for the stationary detector and 5.1 counts for the rotating detector. The rotating signal duration is defined by a FWHM of 7 days.

2. *Positron Background*

Positrons are considered *secondary cosmic rays*, defined as originating from the collisions of other cosmic rays with the interstellar medium (ISM). The dominant production mode for cosmic ray positrons is the inelastic scattering of high energy cosmic ray protons with protons in the ISM [162]. Positrons (and secondary electrons) are the final stable products of hadronic decays resulting from these high energy pp collisions. Cosmic ray propagation models predict a power-law positron energy spectrum with $E^3\Phi$ peaked around 5 GeV (Φ being the positron flux), which is in agreement with low-energy data from experiments like AMS, PAMELA, and Fermi-LAT [134]. The high-energy positron excess observed by these experiments [134, 163, 164] is theorized to be of *primary* origin from either dark matter annihilation [165] or pair-production in pulsar magnetic fields [166].

We are only concerned with the well-measured low-energy positron background below $\mathcal{O}(10\,\mathrm{GeV})$, because positrons with $Q \gtrsim 10\,\mathrm{GeV}$ are only produced in abundance by PBHs with masses below 10^{13} g. Temporal fluctuations of the $(e^- + e^+)$ cosmic ray spectrum were shown to vanish sharply when Voyager 1 crossed the heliopause and left the Solar System in 2012 [167]; however, Voyager still measures time-dependent, anisotropic features in the flux after episodes of solar activity [168]. We infer that the dominant source of background for

temporal positron fluctuations—both periodic and irregular—is solar activity. Low-energy secondary positrons have well-measured and energy-dependent temporal fluctuations within the Solar System. (See Fig. 13.) Large-amplitude fluctuations track the the 11-year solar cycle and small-amplitude fluctuations have been reported with periods matching the 27-day Bartels' rotation of the Sun relative to the Earth [123]. The time-scales of the longest PBH transits considered here are on the order of weeks, implying that periodic fluctuations on the order of months or years can be neglected when simulating time-dependent background for such transits.

We therefore focus on sampling the observed energy-dependent Gaussian noise to construct the positron background. We account for the fact that the mean flux and standard deviation of the flux for the underlying Gaussian noise are both energy-dependent and time-dependent (dominated by the 11-year solar cycle). See Fig. 13. The mean fluxes and standard deviations for a given energy bin are lowest during the period of "solar minimum" ($t \sim 1000\,\mathrm{days}$) and largest during "solar maximum" ($t \sim 4000\,\mathrm{days}$). This modulation is strongest for positrons with $Q \lesssim 1\,\mathrm{GeV}$, and approximately negligible for $Q \gtrsim 10\,\mathrm{GeV}$. The procedure to simulate the time-dependent positron background using published AMS integrated positron flux data for energies $500\,\mathrm{MeV} \leq Q \leq 1\,\mathrm{TeV}$ and temporal daily flux data for energies $1\,\mathrm{GeV} \leq Q \leq 41.9\,\mathrm{GeV}$ from Refs. [123, 134] is described below.

For each PBH transit, positron fluxes at different energies are sampled from distinct Gaussian distributions, converted to particle counts, and summed together to form an energy-integrated background for the energy range $[Q_{\rm min}, Q_{\rm max}]$. For the ith energy bin of width ΔE_i and characteristic energy $\tilde{E}_i$, we calculate the mean positron background count rate as measured by our detector, $\langle \zeta_{{\rm bkgd},i} \rangle$ with units s^{-1}:

$$\langle \zeta_{{\rm bkgd},i} \rangle = \phi_i \, a(\tilde{E}_i) \, \Delta E_i \, \tau_{\rm obs}(\tilde{E}_i). \tag{49}$$

Here ϕ_i is the flux for the ith bin in $\mathrm{m}^{-2}\,\mathrm{sr}^{-1}\,\mathrm{GeV}^{-1}\,\mathrm{s}^{-1}$ as reported by the AMS Collaboration in Ref. [134], a is the detector acceptance, and $\tau_{\rm obs}$ is the observation time fraction discussed in the previous section to account for the geomagnetic cutoff. (The flux ϕ_i should not be confused with the PBH number distribution $\phi(M)$.)

Whereas the mean of the Gaussian noise distribution for each bin $\langle \zeta_{{\rm bkgd},i} \rangle$ can be computed via Eq. (49), the most important quantities to model are the standard deviations σ_i of the fluxes for each bin. The SNR of a PBH transit signal is defined as

$$\mathrm{SNR} \equiv \frac{\mathcal{A}_{\rm max}^2}{\sigma_n^2}, \tag{50}$$

where $\mathcal{A}_{\rm max}$ is the signal amplitude and σ_n is the standard deviation of the total energy-integrated temporal noise in the simulated background. Because the total noise is the sum of normally distributed random variables, we expect that σ_n takes the form

$$\sigma_n = \sqrt{\sum_i \sigma_i^2}\,. \tag{51}$$

Therefore the SNR, and thereby the PBH detection efficiency, is determined by the variances of all the bins enclosed in the interval $[Q_{\rm min}, Q_{\rm max}]$.

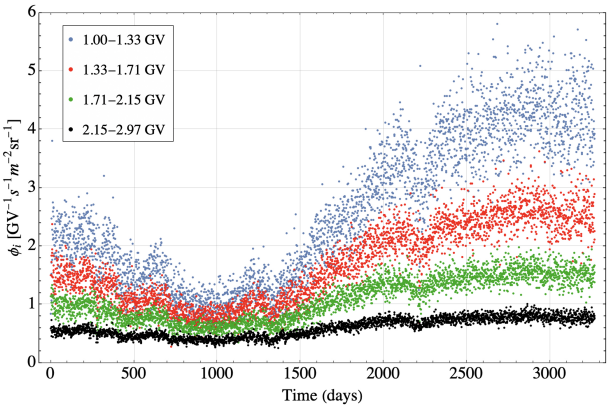


Figure 13: AMS positron daily fluxes collected over approximately 9 years of observation. The data displays a period of 11 years, corresponding to the 11 year solar cycle. Solar modulation effects are most prominent for low energy positrons. We plot the four reported lowest energy bins.

For each energy bin i, we use 100-day running averages to compute the average μ_i and the standard deviation σ_i as functions of time, and determine the minimum and maximum values of σ_i/μ_i for each energy bin. The global minimum and maximum values of this ratio over all 12 energy bins are $(\sigma/\mu)_{\rm min} = 0.063$ and $(\sigma/\mu)_{\rm max} = 0.263$. Thus, for some energy bin i, a conservative estimate for the standard deviation of the fluxes at solar minimum and solar maximum are $\sigma_{i,\rm min} = \langle \zeta_{{\rm bkgd},i} \rangle (\sigma/\mu)_{\rm min}$ and $\sigma_{i,\rm max} = \langle \zeta_{{\rm bkgd},i} \rangle (\sigma/\mu)_{\rm max}$, respectively. Monte Carlo simulations assuming the "noise ratio" or 0.63 or 0.263 form the upper and lower bounds on the shaded regions in Fig. 16 and the black lines are computed assuming the central value 0.163.

To generate a daily flux background for each energy bin, we therefore sample from a Gaussian with mean $\langle \zeta_{{\rm bkgd},i} \rangle$, calculated according to Eq. (49), and standard deviation σ_i. We then convert the fluxes to counts and sum over all energy bins in the range $[Q_{\rm min}, Q_{\rm max}]$. An example of a sampled background superposed with the simulated PBH signal is shown in Fig. 14 (green points).

3. *PBH Detection*

Given that we can generate a PBH e^+ signal according to Sec. III B 1 and sample the time-series background according to Sec. III B 2, we now develop a matched filter technique to detect low-SNR PBH transit signals and estimate time of closest approach. We estimate the theoretical maximum detection

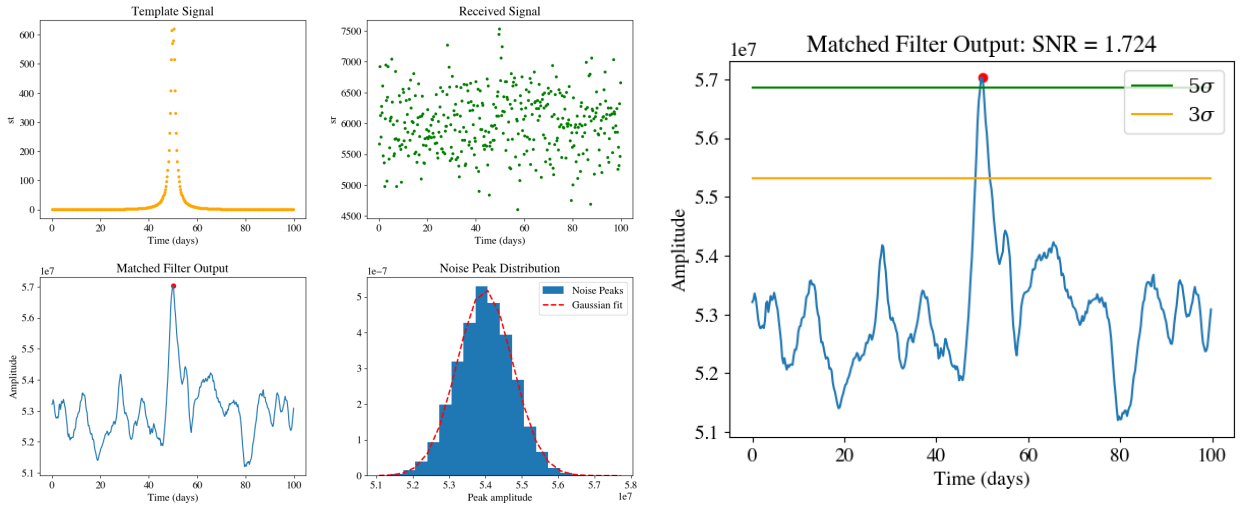


Figure 14: An example showing the intermediate steps for determining the time of closest approach and statistical significance of the matched filter output for a PBH transit event. This event had parameters $M(t_0) = 5.2 \times 10^{13}\,\mathrm{g}$ and $b = 0.15\,\mathrm{AU}$ and was considered a positive detection with significance above the 5σ threshold. The first panel (orange) shows the template signal counts binned on intervals of 0.25 days. The second panel (green) shows the net received signal: the sum of the signal and noise. The histogram plots the peak amplitude distribution obtained by filtering 10^4 days of noise. A gaussian fit is used to compute the noise peak standard deviation σ; a PBH event detection is considered significant if its amplitude exceeds 5σ. A fit to the peak of the matched filter output (right panel, red point) identifies the estimated time of closest approach t_0. Horizontal lines indicate 3σ and 5σ thresholds.

efficiency for PBH transits by a detector configuration by running the matched filter with a known template signal. This allows us to compute maximum detectable impact parameter $b_{\mathrm{max}}(M)$ for the detector and therefore to estimate the annual number of detectable PBH transits for any given PBH mass function model.

A *matched filter* is defined as the optimal linear filter to maximize SNR, as defined in Eq, (50). The input to the filter is the received signal:

$$s_r(t) = s_t(t - t_0) + n(t), \tag{52}$$

where $s_t(t - t_0) \equiv \zeta_{e^+}(t - t_0)$ is the PBH signal defined in Eq. (45) peaked at time of closest approach t_0 and is referred to as the *template signal*. The time-dependent noise background $n(t)$ is generated by the sampling process discussed in Sec. III B 2. The matched filter $\mathcal{H}(t)$ is defined as the conjugate of the scaled, time-reversed and time-shifted template signal,

$$\mathcal{H}(t) = K s_t^*(t_0 - t), \tag{53}$$

where the scaling constant K is typically set to 1.

The output of the matched filter, $s_o(t)$, is the convolution of $\mathcal{H}(t)$ and $s_r(t)$:

$$s_o(t) = \mathcal{F}^{-1}\{\mathcal{F}\{\mathcal{H}(t)\} \times \mathcal{F}\{s_r(t)\}\}, \tag{54}$$

where $\mathcal{F}$ denotes the Fourier transform.

To determine whether a PBH transit signature is present in a simulated received signal dataset $s_r(t)$ and to estimate the time of closest approach, we first construct the matched filter $\mathcal{H}(t)$ given the transit parameters $M, b,$ and v. We apply the filter by convolving $s_r(t)$ with $\mathcal{H}(t)$ and perform peak detection on the filtered output $s_o(t)$ to estimate the amplitude and location of the largest peak. We then perform a numerical Monte Carlo study to simulate the peak amplitude distribution generated by running $\mathcal{O}(10^4)$ days of simulated noise through the filter $\mathcal{H}(t)$. The detected peak in the filtered output $s_o(t)$ is compared to this distribution of amplitudes generated by the noise Monte Carlo study and accepted as a positive detection if its amplitude exceeds a 5σ threshold. Figure 14 shows the results of a matched filter analysis and significance study for a simulated PBH transit with parameters $M = 5.2 \times 10^{13}\,\mathrm{g}$, $b = 0.15\,\mathrm{AU}$, and $v = 246\,\mathrm{km/s}$ and with the temporal counts binned every 0.25 days. This example has an SNR of 1.74 and is detected at a significance level above 5σ using a known template signal.

4. *Maximum Impact Parameters*

The goal of developing this matched filter signal detection technique is to run numerical studies to estimate an upper bound on the PBH detection efficiency of an idealized orbiting detector for a given set of transit parameters (M, b). Note that we define detection efficiency to be the fraction of PBHs with transit parameters (M, b) which are detected above the 5σ level by our detector. Our results are an upper bound on detection efficiency because the matched filter uses a template signal where parameters $M, b,$ and v are known.

Given that we can use numerical studies to determine de-

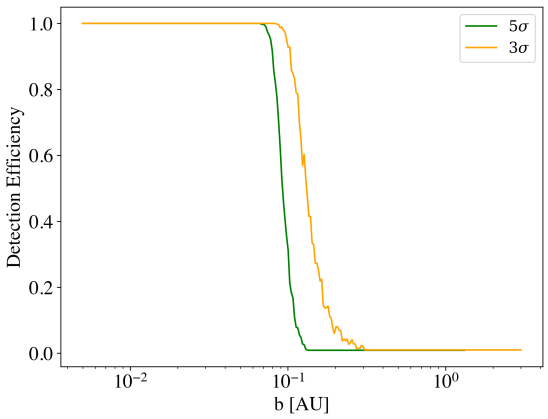


Figure 15: PBH detection efficiency as a function of impact parameter b for PBHs with mass $M(t_0) = 10^{14}\,\mathrm{g}$ assuming the AMS detector configuration. Detection efficiency is computed numerically via Monte Carlo simulations for two different significance levels, 3σ and 5σ. The maximum impact parameter $b_{\max} = (6.68 \pm 0.07) \times 10^{-2}\,\mathrm{AU}$ is defined as the value of b for which the detection efficiency is 99% for the 5σ curve.

tection efficiency, as plotted for example parameters $M = 10^{14}\,\mathrm{g}$, $b = 0.15\,\mathrm{AU}$ in Fig. 15, we may next determine a *maximum impact parameter* function, $b_{\max}(M)$, for each detector configuration. We define $b_{\max}$ as the largest impact parameter such that a PBH with mass $M(t_0)$ can be detected by a given detector geometry at 5σ significance with 99% efficiency. The general steps followed to calculate $b_{\max}$ for a specified value of $M(t_0)$ are: (1) simulate $\mathcal{O}(10^4)$ days of background, (2) for a given value of b, generate the optimal filter $\mathcal{H}(t|M, b, v)$, (3) run the noise through the filter $\mathcal{H}(t)$ to generate a background peak amplitude distribution, (4) simulate 1000 PBH transits with the given b value and determine filtered peak amplitude significance for each one, (5) compute detection efficiency (the fraction of the 1000 transits which are detected at or above the 5σ level), (6) repeat steps 2-4 for impact parameters in the range $[10^{-3}\,\mathrm{AU}, 10^{2}\,\mathrm{AU}]$, (7) identify $b_{\max}(M)$ as the value of b at which detection efficiency drops below 99%. Figure 15 plots detection efficiency as a function of impact parameter b for PBH mass $M(t_0) = 10^{14}\,\mathrm{g}$ using two different significance thresholds and assuming the AMS detector configuration.

Figure 16 plots $b_{\max}(M)$ for masses $5 \times 10^{12}\,\mathrm{g} \leq M(t_0) \leq 10^{17}\,\mathrm{g}$ for the three detector configurations. For the AMS detector configuration (red), the maximum impact parameter drops below $10^{-2}\,\mathrm{AU}$ for $M(t_0) \approx 2 \times 10^{14}\,\mathrm{g}$. The predominant limitation that prevents AMS from being sensitive to transiting PBHs with masses $M > M_*$ is the energy range of AMS positron data. Because $Q_{\min} = 500\,\mathrm{MeV}$, AMS will only be sensitive to PBHs with secondary positron spectra that peak above $500\,\mathrm{MeV}$. Secondary emission spectra typically peak at an energy $Q_{\mathrm{peak}} \approx 5T$ for a PBH of temperature T. Thus, AMS should only be sensitive to PBHs with temperatures $T \gtrsim 100\,\mathrm{MeV}$, which corresponds to $M(t_0) \lesssim 10^{14}\,\mathrm{g}$, which is reflected in our result.

The maximum impact parameter curves in Fig. 16 for the $Q_{\min} = 50\,\mathrm{MeV}$ (blue) and $Q_{\min} = 5\,\mathrm{MeV}$ (green) datasets show more complex behavior and admit detectable PBHs up to $\sim 3 \times 10^{15}\,\mathrm{g}$ and $\sim 3 \times 10^{16}\,\mathrm{g}$, respectively. Both curves feature a local minimum around $10^{14}\,\mathrm{g}$. This is due to the energy-dependent noise peaking around $1\,\mathrm{GeV}$—about the temperature of a $10^{14}\,\mathrm{g}$ black hole. PBHs with secondary positron spectra that peak near $1\,\mathrm{GeV}$ thus have noisier background than those peaked at lower energies. Furthermore, positron Hawking spectra that peak around $T = 1\,\mathrm{GeV}$ have lower integrated emission rates than PBHs with temperatures $T \gg 1\,\mathrm{GeV}$ due to the decrease of $\dot{N}(M)$ with energy. These features of the Hawking spectra and positron background result in a local minimum around $M = 10^{14}\,\mathrm{g}$. The subsequent turnover of the curves observed at $\sim 10^{15}\,\mathrm{g}$ and $\sim 10^{16}\,\mathrm{g}$ (respectively) corresponds to the positron Hawking spectrum peak occurring at energies $Q < Q_{\min}$ for each dataset, thus resulting in low signal counts.

5. *Sensitivity to PBH Models*

Using the values of $b_{\max}(M)$ shown in Fig. 16 from our numerical studies, we can produce an updated version of Fig. 9, which now plots an upper bound on the number of *detectable* $e^{\pm}$-producing PBH transits per year for each detector configuration as a function of LN and GCC model parameters. We compute the detectable PBH transit rate by replacing the $b_{\max}$ integration bound of Eq. (40) with the mass dependent $b_{\max}(M)$. The number of detectable transits per year is then

$$\bar{\Phi}^{\mathrm{det.}}_{e^{\pm}} = \rho^{\odot}_{\mathrm{DM}} \int_0^{5\times10^{17}\,\mathrm{g}} \frac{dM}{M} \psi(M, t_0) \bar{v} \pi b^2_{\max}(M), \quad (55)$$

which is integrated numerically by interpolating the $b_{\max}(M)$ values shown as black points in Fig. 16 and using the LN and GCC mass functions $\psi(M, t_0)$ defined in Section II B 1.

Figure 17 plots $\bar{\Phi}^{\mathrm{det.}}_{e^{\pm}}$ for regions of LN and GCC parameter with $\bar{M}_i > M_*$ for all three detector configurations, labeled by their respective $Q_{\min}$ values. With 10 years of time-dependent positron flux data, the AMS experiment could constrain very small regions of both extended mass function model parameter spaces. The main difficulty that prevents AMS from probing a larger region of parameter space is its high value of $Q_{\min} = 500\,\mathrm{MeV}$, which limits its sensitivity to PBHs with temperatures $T \gtrsim 100\,\mathrm{MeV}$ or, equivalently, masses $M \lesssim 10^{14}\,\mathrm{g}$. The hypothetical $Q_{\min} = 50\,\mathrm{MeV}$ and $Q_{\min} = 5\,\mathrm{MeV}$ positron datasets (rows 2 and 3 of Fig. 17) would be capable of probing much larger regions of parameter space.

For the geosynchronous detector configuration, we recompute $b_{\max}(M)$ assuming all AMS detector parameters held constant except $Q_{\min} = 50\,\mathrm{MeV}$, $\tau_{\mathrm{obs}} = 1$ for all Q, and orbital period $\tau = 1$ day. (See the blue curve in Fig. 16.) We then use this mass-dependent integration bound in Eq. (40) to compute the number of detectable transits per year given a set

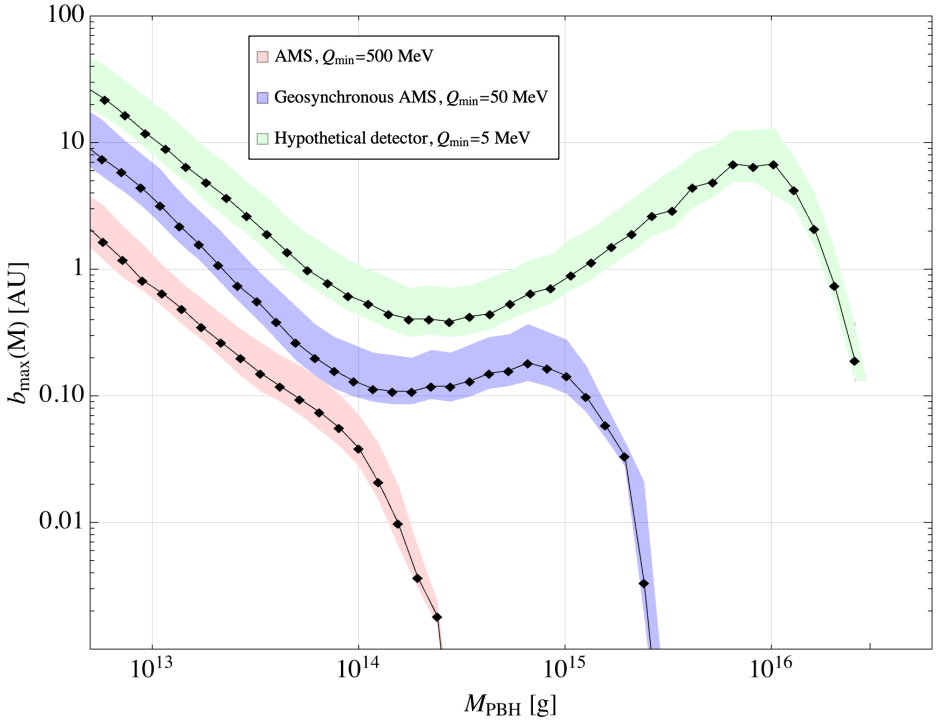


Figure 16: Maximum impact parameter as a function of PBH mass $M(t_0)$ for three datasets: the AMS experiment with $Q_{\rm min} = 500\,{\rm MeV}$ (red), AMS in geosynchronous orbit with $Q_{\rm min} = 50\,{\rm MeV}$ (blue), and a hypothetical detector with AMS acceptance unchanged but $Q_{\rm min} = 5\,{\rm MeV}$ and no geomagnetic field (green). Data points in this figure are results of the numerical studies described in Sec. III B 4. Lines are to guide the eye. AMS would only be sensitive to PBHs with masses $M(t_0) \lesssim 10^{14}\,{\rm g}$ due to its relatively high lower threshold energy for detecting positrons. Note that the Earth-Moon distance is about $0.0025\,{\rm AU}$. The lower and upper bounds on the shaded regions correspond to assuming either solar maximum or solar minimum conditions, respectively, when simulating the time-dependent positron background. Black lines and points are computed assuming the central value for the noise fraction between solar maximum and minimum.

of mass function model parameters. The results for this hypothetical dataset are shown as the middle row of contour plots in Fig. 17.

Finally, we repeat the analysis for a hypothetical detector that has equivalent precision and acceptance to AMS but is fully outside the Earth's magnetosphere, and hence would be sensitive to positrons with energies $Q \geq Q_{\rm min} = 5\,{\rm MeV}$. Contour plots of detectable transit rates $\bar{\Phi}^{\rm det.}_{e^\pm}$ for this detector configuration are shown in the bottom row of Fig. 17. This simulated dataset is capable of probing PBH mass functions peaked in the asteroid mass range ($\bar{M}_i \gtrsim 2 \times 10^{17}\,{\rm g}$) even though maximum impact parameters only exceed $10^{-3}\,{\rm AU}$ for $M \leq 3 \times 10^{16}\,{\rm g}$ (see the green curve in Fig. 16), because extended mass functions have a low-mass tail which yields a nontrivial subpopulation of PBHs with mass $M \leq \bar{M}_i$.

IV. CONCLUSION

In order to close the unconstrained asteroid-mass window in PBH mass parameter space, new detection signatures are required. We demonstrate a novel method of analyzing time-series cosmic ray positron data to look for evidence of PBHs transiting past Earth through the inner Solar System. Positrons are a particularly promising signature due to their low astrophysical backgrounds and the high precision and long observation time period of AMS data. We have shown that if PBHs obey a realistic extended mass function $\psi(M_i)$ that is peaked at $\bar{M}_i \geq 2 \times 10^{17}\,{\rm g}$, for which $f_{\rm PBH} = 1$ remains viable in the light of existing observations and constraints [7–15] , then we should expect $\mathcal{O}(3)$ or fewer transits per year to pass within $1\,{\rm AU}$ of the Earth. These high transit rates motivate us to simulate the time-dependent positron signature measured by an experiment like AMS in LEO during a PBH transit.

We find that AMS would not be sensitive to PBHs with present-day masses $M(t_0) \gtrsim 2 \times 10^{14}\,{\rm g}$ because of its sensitivity to positron energies $Q \geq Q_{\rm min} = 500\,{\rm MeV}$. We have demonstrated that this new technique may be effective, however, if applied to a dataset that reaches down to low enough positron energies to probe the larger-mass PBHs that may exist today. In order to probe PBH mass functions that peak below $\bar{M}_i \leq 5 \times 10^{17}\,{\rm g}$, we would need time-dependent positron flux data from at least several years of observations spanning energies from approximately $5\,{\rm MeV} - 1\,{\rm GeV}$. To collect such low-rigidity positrons would require that the instrument be located outside the Earth's magnetosphere. If a positron detector

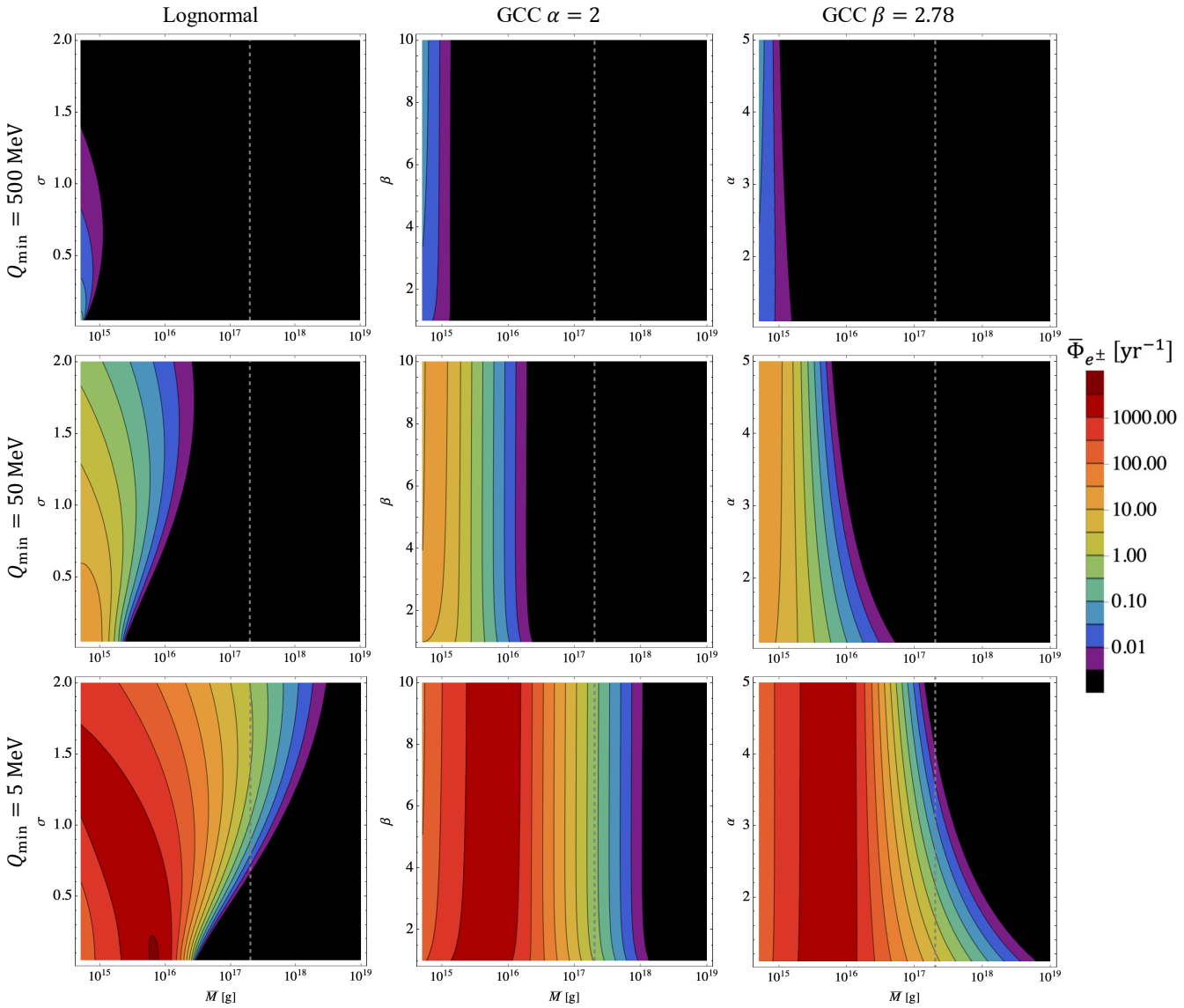


Figure 17: Total number of detectable $e^{\pm}$-producing PBH transits per year as a function of $\bar{M}_i$ at PBH formation time for three simulated datasets: AMS, which is sensitive to positrons with energies $Q \geq Q_{\rm min} = 500\,{\rm MeV}$ (top row), AMS in geosynchronous orbit, sensitive to positrons with $Q \geq Q_{\rm min} = 50\,{\rm MeV}$ (middle row), and a non-rotating AMS-like detector beyond the geomagnetic field with $Q_{\rm min} = 5\,{\rm MeV}$. Note that we define a "detectable" transit to be a PBH of mass $M(t_0)$ transiting with impact parameter $b \leq b_{\rm max}(M)$, as plotted in Fig. 16. For all models with $\bar{M}_i \geq 2 \times 10^{17}\,{\rm g}$ (vertical dashed gray line), $f_{\rm PBH} = 1$ is allowed by existing Hawking emission constraints on extended mass functions [15, 62].

with similar precision and acceptance as AMS were placed in an orbit such that it could reliably detect positrons with energies above a lower threshold of 5 MeV, then a few years' worth of data could either place strong constraints on PBH mass functions peaked in the as-yet unconstrained "asteroid-mass" window, or yield the first-ever positive detection of a PBH and its tell-tale Hawking emission.

Because such a dataset does not currently exist, we plan to extend our current work to analyze the prospects for PBH detection with data from the PAMELA cosmic ray detector, which reported positron fluxes down to 50 MeV [169]—an energy range accessible due to its quasi-polar orbit at 70^o inclination. The most significant future work, however, will include a generalization of this analysis procedure to both γ-ray and X-ray cosmic ray datasets to probe heavier, colder PBHs. We also intend to further develop the parameter estimation techniques discussed in this work in order to analyze real cosmic ray data and search for signals of PBHs in our own Solar System.

Additional next steps include usingour simulation code to determine the optimal detector parameters, orbit, and particle energy ranges such that a purpose-built instrument could

probe the largest range of PBH masses and therefore the largest region of model parameter space. This result could be used to inform the design of future cosmic ray experiments with the aim of detecting Hawking radiation from PBHs.

Additionally, detecting local PBH transits affords a variety of possible multi-messenger signals, which should be leveraged to both confirm the observation of PBH candidates and to search a wider parameter space than what is accessible via only one signature. In addition to the gravitational-perturbation signatures mentioned above [65, 66, 144, 146, 148], one could also consider detectable γ-ray, X-ray, and neutrino fluxes from Hawking radiation. Given our focus here on positron-producing PBHs, a natural companion signature to consider would be high-energy photons at $E_\gamma \geq m_e = 511\,\mathrm{keV}$. Current constraints on PBH number density from isotropic fluxes of 511 keV photons already place strong constraints on extended mass functions up to $\mathcal{O}(10^{17})\,\mathrm{g}$ [170, 171].

We may estimate an upper bound on the possible 511 keV photon flux from the PBH transits discussed in this article. The secondary photon emission spectra for a PBH with $M = 10^{15}\,\mathrm{g}$—approximately the lightest and hottest PBH that could still exist today—is of the order $d^2N^{(2)}_{511}/dtdQ \sim 10^{22}\,\mathrm{GeV}^{-1}\mathrm{s}^{-1}$. This serves as an upper bound on the emitted flux at 511 keV for all PBHs with $M < 10^{15}\,\mathrm{g}$ because heavier PBHs produce fewer secondary particles.

If a PBH with $M = 10^{15}\,\mathrm{g}$ were to transit past Earth with an impact parameter of 1 AU, the expected flux of 511 keV photons at Earth would be $\Phi_{511} = 1.8 \times 10^{-5}\,\mathrm{m}^{-2}\mathrm{s}^{-1}$. The reported isotropic background flux at 511 keV is $\mathcal{O}(10^{-2})\,\mathrm{m}^{-2}\mathrm{s}^{-1}$, indicating that the signal count rate would be about 1000 times smaller than the background. However, a γ-ray experiment with good angular resolution pointed at the transiting PBH may be able to detect it as a localized point-source. Application of a matched filter analysis, such as that described in this article, to time-series photon data would be an important technique with which to extract transit signals from low-SNR data.

ACKNOWLEDGMENTS

We are grateful to Bryce Cyr, Benjamin Lehmann, Vincent Vennin, and Rainer Weiss for helpful discussions. This material is based upon work supported by the National Science Foundation Graduate Research Fellowship under Grant No. 2141064. Portions of this work were conducted in MIT's Center for Theoretical Physics – a Leinweber Institute and partially supported by the U.S. Department of Energy under Contract No. DE-SC0012567.

[1] Ya. B. Zel'dovich and I. D. Novikov, "The Hypothesis of Cores Retarded during Expansion and the Hot Cosmological Model," Astronomicheskii Zhurnal **43**, 758 (1966).
[2] Stephen Hawking, "Gravitationally collapsed objects of very low mass," Mon. Not. Roy. Astron. Soc. **152**, 75 (1971).
[3] B. J. Carr and S. W. Hawking, "Black Holes in the Early Universe," Mon. Not. Roy. Astron. Soc. **168**, 399–415 (1974).
[4] Bernard J. Carr, "Some cosmological consequences of primordial black-hole evaporations," Astrophys. J. **206**, 8–25 (1976).
[5] M. Yu. Khlopov, B. A. Malomed, Ia. B. Zeldovich, and Ya. B. Zeldovich, "Gravitational instability of scalar fields and formation of primordial black holes," Mon. Not. Roy. Astron. Soc. **215**, 575–589 (1985).
[6] Maxim Yu. Khlopov, "Primordial Black Holes," Res. Astron. Astrophys. **10**, 495–528 (2010), arXiv:0801.0116 [astro-ph].
[7] Albert Escrivà, Florian Kühnel, and Yuichiro Tada, "Primordial black holes," in *Black Holes in the Era of Gravitational-Wave Astronomy*, edited by Manuel Arca Sedda, Elisa Bortolas, and Mario Spera (2024) pp. 261–377, arXiv:2211.05767 [astro-ph.CO].
[8] B. J. Carr, Kazunori Kohri, Yuuiti Sendouda, and Jun'ichi Yokoyama, "New cosmological constraints on primordial black holes," Phys. Rev. D **81**, 104019 (2010), arXiv:0912.5297 [astro-ph.CO].
[9] Bernard Carr and Florian Kuhnel, "Primordial Black Holes as Dark Matter: Recent Developments," Ann. Rev. Nucl. Part. Sci. **70**, 355–394 (2020), arXiv:2006.02838 [astro-ph.CO].
[10] Bernard Carr, Kazunori Kohri, Yuuiti Sendouda, and Jun'ichi Yokoyama, "Constraints on primordial black holes," Rept. Prog. Phys. **84**, 116902 (2021), arXiv:2002.12778 [astro-ph.CO].
[11] Bernard Carr and Florian Kuhnel, "Primordial black holes as dark matter candidates," SciPost Phys. Lect. Notes **48**, 1 (2022), arXiv:2110.02821 [astro-ph.CO].
[12] Ogan Özsoy and Gianmassimo Tasinato, "Inflation and Primordial Black Holes," Universe **9**, 203 (2023), arXiv:2301.03600 [astro-ph.CO].
[13] Anne M. Green and Bradley J. Kavanagh, "Primordial Black Holes as a dark matter candidate," J. Phys. G **48**, 043001 (2021), arXiv:2007.10722 [astro-ph.CO].
[14] Bernard Carr, Sebastien Clesse, Juan Garcia-Bellido, Michael Hawkins, and Florian Kuhnel, "Observational evidence for primordial black holes: A positivist perspective," Phys. Rept. **1054**, 1–68 (2024), arXiv:2306.03903 [astro-ph.CO].
[15] Matthew Gorton and Anne M. Green, "How open is the asteroid-mass primordial black hole window?" (2024), arXiv:2403.03839 [astro-ph.CO].
[16] M. Aguilar *et al.* (AMS), "The Alpha Magnetic Spectrometer (AMS) on the international space station: Part II — Results from the first seven years," Phys. Rept. **894**, 1–116 (2021).
[17] Sebastien Clesse and Juan Garcia-Bellido, "GW190425, GW190521 and GW190814: Three candidate mergers of primordial black holes from the QCD epoch," Phys. Dark Univ. **38**, 101111 (2022), arXiv:2007.06481 [astro-ph.CO].
[18] Qing-Guo Huang, Chen Yuan, Zu-Cheng Chen, and Lang Liu, "GW230529_181500: a potential primordial binary black hole merger in the mass gap," JCAP **08**, 030 (2024), arXiv:2404.05691 [gr-qc].
[19] R. Abbott *et al.* (KAGRA and VIRGO and LIGO Scientific Collaborations), "GWTC-3: Compact Binary Coalescences Observed by LIGO and Virgo during the Second Part of the Third Observing Run," Phys. Rev. X **13**, 041039 (2023), arXiv:2111.03606 [gr-qc].
[20] R. Abbott *et al.* (LIGO Scientific, Virgo), "GW190521: A Bi-

nary Black Hole Merger with a Total Mass of $150 M_\odot$," Phys. Rev. Lett. **125**, 101102 (2020), arXiv:2009.01075 [gr-qc].
[21] Khun Sang Phukon *et al.*, "The hunt for sub-solar primordial black holes in low mass ratio binaries is open," (2021), arXiv:2105.11449 [astro-ph.CO].
[22] Gonzalo Morras *et al.*, "Analysis of a subsolar-mass compact binary candidate from the second observing run of Advanced LIGO," Phys. Dark Univ. **42**, 101285 (2023), arXiv:2301.11619 [gr-qc].
[23] R. Abbott *et al.* (LVK), "Search for subsolar-mass black hole binaries in the second part of Advanced LIGO's and Advanced Virgo's third observing run," Mon. Not. Roy. Astron. Soc. **524**, 5984–5992 (2023), [Erratum: Mon.Not.Roy.Astron.Soc. 526, 6234 (2023)], arXiv:2212.01477 [astro-ph.HE].
[24] B. P. Abbott *et al.* (LIGO Scientific, Virgo), "Search for Subsolar-Mass Ultracompact Binaries in Advanced LIGO's First Observing Run," Phys. Rev. Lett. **121**, 231103 (2018), arXiv:1808.04771 [astro-ph.CO].
[25] Marco Castellano *et al.*, "Early Results from GLASS-JWST. III. Galaxy Candidates at z 9-15," Astrophys. J. Lett. **938**, L15 (2022), arXiv:2207.09436 [astro-ph.GA].
[26] Marco Castellano *et al.*, "Early Results from GLASS-JWST. XIX. A High Density of Bright Galaxies at z $\approx$ 10 in the A2744 Region," Astrophys. J. Lett. **948**, L14 (2023), arXiv:2212.06666 [astro-ph.GA].
[27] N. J. Adams *et al.*, "Discovery and properties of ultra-high redshift galaxies ($9 < z < 12$) in the JWST ERO SMACS 0723 Field," Mon. Not. Roy. Astron. Soc. **518**, 4755–4766 (2023), arXiv:2207.11217 [astro-ph.GA].
[28] Hakim Atek *et al.*, "Revealing galaxy candidates out to z 16 with JWST observations of the lensing cluster SMACS0723," Mon. Not. Roy. Astron. Soc. **519**, 1201–1220 (2023), arXiv:2207.12338 [astro-ph.GA].
[29] Yuichi Harikane *et al.*, "A Comprehensive Study of Galaxies at z $\sim$ 9–16 Found in the Early JWST Data: Ultraviolet Luminosity Functions and Cosmic Star Formation History at the Pre-reionization Epoch," Astrophys. J. Suppl. **265** (2023), 10.3847/1538-4365/acaaa9, arXiv:2208.01612 [astro-ph.GA].
[30] Rohan P. Naidu *et al.*, "Two Remarkably Luminous Galaxy Candidates at z $\approx$ 10-12 Revealed by JWST," Astrophs. J. Lett. **940**, L14 (2022), arXiv:2207.09434 [astro-ph.GA].
[31] Akos Bogdan *et al.*, "Evidence for heavy-seed origin of early supermassive black holes from a z $\approx$ 10 X-ray quasar," Nature Astron. **8**, 126–133 (2024), arXiv:2305.15458 [astro-ph.GA].
[32] Priyamvada Natarajan, Fabio Pacucci, Angelo Ricarte, Akos Bogdan, Andy D. Goulding, and Nico Cappelluti, "First Detection of an Overmassive Black Hole Galaxy UHZ1: Evidence for Heavy Black Hole Seed Formation from Direct Collapse," Astrophys. J. Lett. **960**, L1 (2024), arXiv:2308.02654 [astro-ph.HE].
[33] Orsolya E. Kovacs *et al.*, "A Candidate Supermassive Black Hole in a Gravitationally Lensed Galaxy at Z $\approx$ 10," Astrophys. J. Lett. **965**, L21 (2024), arXiv:2403.14745 [astro-ph.GA].
[34] Rebecca L. Larson *et al.*, "A CEERS Discovery of an Accreting Supermassive Black Hole 570 Myr after the Big Bang: Identifying a Progenitor of Massive $z > 6$ Quasars," Astrophys. J. Lett. **953**, L29 (2023), arXiv:2303.08918 [astro-ph.GA].
[35] Roberto Maiolino *et al.*, "A small and vigorous black hole in the early Universe," (2024), [Erratum: Nature 630, E2 (2024)], arXiv:2305.12492 [astro-ph.GA].
[36] N. Menci, M. Castellano, P. Santini, E. Merlin, A. Fontana, and F. Shankar, "High-redshift Galaxies from Early JWST Observations: Constraints on Dark Energy Models," Astrophys. J. Lett. **938**, L5 (2022), arXiv:2208.11471 [astro-ph.CO].
[37] A. D. Dolgov, "Solution of JWST and HST Problems by Primordial Black Holes," (2024), arXiv:2401.06882 [astro-ph.CO].
[38] Gert Hütsi, Martti Raidal, Juan Urrutia, Ville Vaskonen, and Hardi Veermäe, "Did JWST observe imprints of axion miniclusters or primordial black holes?" Phys. Rev. D **107**, 043502 (2023), arXiv:2211.02651 [astro-ph.CO].
[39] Joseph Silk, Mitchell C. Begelman, Colin Norman, Adi Nusser, and Rosemary F. G. Wyse, "Which Came First: Supermassive Black Holes or Galaxies? Insights from JWST," Astrophys. J. Lett. **961**, L39 (2024), arXiv:2401.02482 [astro-ph.GA].
[40] Boyuan Liu and Volker Bromm, "Accelerating Early Massive Galaxy Formation with Primordial Black Holes," Astrophys. J. Lett. **937**, L30 (2022), arXiv:2208.13178 [astro-ph.CO].
[41] N. Aghanim *et al.* (Planck), "Planck 2018 results. VI. Cosmological parameters," Astron. Astrophys. **641**, A6 (2020), [Erratum: Astron.Astrophys. 652, C4 (2021)], arXiv:1807.06209 [astro-ph.CO].
[42] Antonio Boveia and Caterina Doglioni, "Dark Matter Searches at Colliders," Ann. Rev. Nucl. Part. Sci. **68**, 429–459 (2018), arXiv:1810.12238 [hep-ex].
[43] A. Weltman *et al.*, "Fundamental physics with the Square Kilometre Array," Publ. Astron. Soc. Austral. **37**, e002 (2020), arXiv:1810.02680 [astro-ph.CO].
[44] Prateek Agrawal *et al.*, "Feebly-interacting particles: FIPs 2020 workshop report," Eur. Phys. J. C **81**, 1015 (2021), arXiv:2102.12143 [hep-ph].
[45] Jodi Cooley *et al.*, "Report of the Topical Group on Particle Dark Matter for Snowmass 2021," (2022), arXiv:2209.07426 [hep-ph].
[46] R. L. Workman *et al.* (Particle Data Group), "Review of Particle Physics," PTEP **2022**, 083C01 (2022).
[47] B. Carter, "Charge and particle conservation in black hole decay," Phys. Rev. Lett. **33**, 558–561 (1974).
[48] Elba Alonso-Monsalve and David I. Kaiser, "Primordial Black Holes with QCD Color Charge," Phys. Rev. Lett. **132**, 231402 (2024), arXiv:2310.16877 [hep-ph].
[49] Florian Kuhnel and Tommy Ohlsson, "Decaying Dark Matter in Halos of Primordial Black Holes," Eur. Phys. J. C **79**, 687 (2019), arXiv:1811.05810 [astro-ph.CO].
[50] Florian Kuhnel and Tommy Ohlsson, "Signatures of Compact Halos of Sterile-Neutrino Dark Matter," Phys. Rev. D **96**, 103020 (2017), arXiv:1707.04493 [astro-ph.CO].
[51] S. W. Hawking, "Black hole explosions," Nature **248**, 30–31 (1974).
[52] S. W. Hawking, "Particle Creation by Black Holes," Commun. Math. Phys. **43**, 199–220 (1975), [Erratum: Commun.Math.Phys. 46, 206 (1976)].
[53] Peter Fisher, Hayden Tedrake, Alexandra P. Klipfel, and David I. Kaiser, "A Primal Scream?" In Prep. (2025).
[54] Xavier Boluna, Stefano Profumo, Juliette Blé, and Dana Hennings, "Searching for Exploding black holes," JCAP **04**, 024 (2024), arXiv:2307.06467 [astro-ph.HE].
[55] Michael J. Baker, Joaquim Iguaz Juan, Aidan Symons, and Andrea Thamm, "Could We Observe an Exploding Black Hole in the Near Future?" (2025), arXiv:2503.10755 [hep-ph].
[56] Alexandra P. Klipfel and David I. Kaiser, "Ultra-High-Energy Neutrinos from Primordial Black Holes," (2025), arXiv:2503.19227 [hep-ph].

[57] Michael J. Baker, Joaquim Iguaz Juan, Aidan Symons, and Andrea Thamm, "Explaining the PeV Neutrino Fluxes at KM3NeT and IceCube with Quasi-Extremal Primordial Black Holes," (2025), arXiv:2505.22722 [hep-ph].

[58] Lua F. T. Airoldi, Gustavo F. S. Alves, Yuber F. Perez-Gonzalez, Gabriel M. Salla, and Renata Zukanovich Funchal, "Could a Primordial Black Hole Explosion Explain the KM3NeT Event?" (2025), arXiv:2505.24666 [hep-ph].

[59] Mathieu Boudaud and Marco Cirelli, "Voyager 1 $e^{\pm}$ Further Constrain Primordial Black Holes as Dark Matter," Phys. Rev. Lett. **122**, 041104 (2019), arXiv:1807.03075 [astro-ph.HE].

[60] Jia-Zhi Huang and Yu-Feng Zhou, "Constraints on evaporating primordial black holes from the AMS-02 positron data," Phys. Rev. D **111**, 083525 (2025), arXiv:2403.04987 [hep-ph].

[61] Bing-Yu Su, Xu Pan, Guan-Sen Wang, Lei Zu, Yupeng Yang, and Lei Feng, "Constraining primordial black holes as dark matter using AMS-02 data," Eur. Phys. J. C **84**, 606 (2024), [Erratum: Eur.Phys.J.C 84, 768 (2024)], arXiv:2403.04988 [astro-ph.HE].

[62] Pedro De la Torre Luque, Jordan Koechler, and Shyam Balaji, "Refining Galactic primordial black hole evaporation constraints," Phys. Rev. D **110**, 123022 (2024), arXiv:2406.11949 [astro-ph.HE].

[63] J. L. G. Sobrinho and P. Augusto, "Direct detection of Black Holes via electromagnetic radiation," Mon. Not. Roy. Astron. Soc. **441**, 2878–2884 (2014), arXiv:1406.1785 [astro-ph.CO].

[64] Alexandre Arbey and Jérémy Auffinger, "Detecting Planet 9 via Hawking radiation," (2020), arXiv:2006.02944 [gr-qc].

[65] Tung X. Tran, Sarah R. Geller, Benjamin V. Lehmann, and David I. Kaiser, "Close encounters of the primordial kind: A new observable for primordial black holes as dark matter," Phys. Rev. D **110**, 063533 (2024), arXiv:2312.17217 [astro-ph.CO].

[66] Michal Cuadrat-Grzybowski, Sébastien Clesse, Pascale Defraigne, Michel Van Camp, and Bruno Bertrand, "Probing primordial black holes and dark matter clumps in the Solar System with gravimeter and Global Navigation Satellite Systems networks," Phys. Rev. D **110**, 063029 (2024), arXiv:2403.14397 [astro-ph.CO].

[67] Valentin Thoss and Andreas Burkert, "Primordial Black Holes in the Solar System," Astrophys. J. **980**, 238 (2025), arXiv:2409.04518 [astro-ph.EP].

[68] Don N. Page, "Particle Emission Rates from a Black Hole: Massless Particles from an Uncharged, Nonrotating Hole," Phys. Rev. D **13**, 198–206 (1976).

[69] Don N. Page, "Particle Emission Rates from a Black Hole. 2. Massless Particles from a Rotating Hole," Phys. Rev. D **14**, 3260–3273 (1976).

[70] Don N. Page, "Particle Emission Rates from a Black Hole. 3. Charged Leptons from a Nonrotating Hole," Phys. Rev. D **16**, 2402–2411 (1977).

[71] J. H. MacGibbon and B. R. Webber, "Quark and gluon jet emission from primordial black holes: The instantaneous spectra," Phys. Rev. D **41**, 3052–3079 (1990).

[72] S. A. Teukolsky and W. H. Press, "Perturbations of a rotating black hole. III. Interaction of the hole with gravitational and electromagnetic radiation," Astrophys. J. **193**, 443–461 (1974).

[73] Saul A. Teukolsky, "Perturbations of a rotating black hole. 1. Fundamental equations for gravitational electromagnetic and neutrino field perturbations," Astrophys. J. **185**, 635–647 (1973).

[74] Takeshi Chiba and Shuichiro Yokoyama, "Spin Distribution of Primordial Black Holes," PTEP **2017**, 083E01 (2017), arXiv:1704.06573 [gr-qc].

[75] V. De Luca, G. Franciolini, P. Pani, and A. Riotto, "The evolution of primordial black holes and their final observable spins," JCAP **04**, 052 (2020), arXiv:2003.02778 [astro-ph.CO].

[76] Siri Chongchitnan and Joseph Silk, "Extreme-value statistics of the spin of primordial black holes," Phys. Rev. D **104**, 083018 (2021), arXiv:2109.12268 [astro-ph.CO].

[77] G. W. Gibbons, "Vacuum Polarization and the Spontaneous Loss of Charge by Black Holes," Commun. Math. Phys. **44**, 245–264 (1975).

[78] Gabriel Vasquez, John Kushan, Makana Silva, Emily Koivu, Arijit Das, and Christopher M. Hirata, "Corrections to Hawking radiation from asteroid-mass primordial black holes: description of the stochastic charge effect in quantum electrodynamics," (2024), arXiv:2407.09724 [astro-ph.CO].

[79] Alexandre Arbey and Jérémy Auffinger, "BlackHawk: A public code for calculating the Hawking evaporation spectra of any black hole distribution," Eur. Phys. J. C **79**, 693 (2019), arXiv:1905.04268 [gr-qc].

[80] Alexandre Arbey and Jérémy Auffinger, "Physics Beyond the Standard Model with BlackHawk v2.0," Eur. Phys. J. C **81**, 910 (2021), arXiv:2108.02737 [gr-qc].

[81] Alexandre Arbey and Jeremy Auffinger, "BlackHawk v2.0: A public code for calculating the Hawking evaporation spectra of any black hole distribution," .

[82] Adam Coogan, Logan Morrison, and Stefano Profumo, "Hazma: A Python Toolkit for Studying Indirect Detection of Sub-GeV Dark Matter," JCAP **01**, 056 (2020), arXiv:1907.11846 [hep-ph].

[83] Torbjörn Sjöstrand, Stefan Ask, Jesper R. Christiansen, Richard Corke, Nishita Desai, Philip Ilten, Stephen Mrenna, Stefan Prestel, Christine O. Rasmussen, and Peter Z. Skands, "An introduction to PYTHIA 8.2," Comput. Phys. Commun. **191**, 159–177 (2015), arXiv:1410.3012 [hep-ph].

[84] Bernard Carr, Martti Raidal, Tommi Tenkanen, Ville Vaskonen, and Hardi Veermäe, "Primordial black hole constraints for extended mass functions," Phys. Rev. D **96**, 023514 (2017), arXiv:1705.05567 [astro-ph.CO].

[85] Nicola Bellomo, José Luis Bernal, Alvise Raccanelli, and Licia Verde, "Primordial Black Holes as Dark Matter: Converting Constraints from Monochromatic to Extended Mass Distributions," JCAP **01**, 004 (2018), arXiv:1709.07467 [astro-ph.CO].

[86] Andrew D. Gow, Christian T. Byrnes, and Alex Hall, "Accurate model for the primordial black hole mass distribution from a peak in the power spectrum," Phys. Rev. D **105**, 023503 (2022), arXiv:2009.03204 [astro-ph.CO].

[87] Matthew W. Choptuik, "Universality and scaling in gravitational collapse of a massless scalar field," Phys. Rev. Lett. **70**, 9–12 (1993).

[88] Charles R. Evans and Jason S. Coleman, "Observation of critical phenomena and selfsimilarity in the gravitational collapse of radiation fluid," Phys. Rev. Lett. **72**, 1782–1785 (1994), arXiv:gr-qc/9402041.

[89] Jens C. Niemeyer and K. Jedamzik, "Dynamics of primordial black hole formation," Phys. Rev. D **59**, 124013 (1999), arXiv:astro-ph/9901292.

[90] Carsten Gundlach and Jose M. Martin-Garcia, "Critical phenomena in gravitational collapse," Living Rev. Rel. **10**, 5 (2007), arXiv:0711.4620 [gr-qc].

[91] Ilia Musco, John C. Miller, and Alexander G. Polnarev, "Primordial black hole formation in the radiative era: Investigation of the critical nature of the collapse," Class. Quant. Grav. **26**, 235001 (2009), arXiv:0811.1452 [gr-qc].

[92] Masaru Shibata and Misao Sasaki, "Black hole formation in the Friedmann universe: Formulation and computation in numerical relativity," Phys. Rev. D **60**, 084002 (1999), arXiv:gr-qc/9905064.

[93] Tomohiro Harada, Chul-Moon Yoo, and Yasutaka Koga, "Revisiting compaction functions for primordial black hole formation," Phys. Rev. D **108**, 043515 (2023), arXiv:2304.13284 [gr-qc].

[94] Ilia Musco, "Threshold for primordial black holes: Dependence on the shape of the cosmological perturbations," Phys. Rev. D **100**, 123524 (2019), arXiv:1809.02127 [gr-qc].

[95] Albert Escrivà, Cristiano Germani, and Ravi K. Sheth, "Universal threshold for primordial black hole formation," Phys. Rev. D **101**, 044022 (2020), arXiv:1907.13311 [gr-qc].

[96] Albert Escrivà, "PBH Formation from Spherically Symmetric Hydrodynamical Perturbations: A Review," Universe **8**, 66 (2022), arXiv:2111.12693 [gr-qc].

[97] Bernard J. Carr, "The Primordial black hole mass spectrum," Astrophys. J. **201**, 1–19 (1975).

[98] Jens C. Niemeyer and K. Jedamzik, "Near-critical gravitational collapse and the initial mass function of primordial black holes," Phys. Rev. Lett. **80**, 5481–5484 (1998), arXiv:astro-ph/9709072.

[99] Anne M. Green and Andrew R. Liddle, "Critical collapse and the primordial black hole initial mass function," Phys. Rev. D **60**, 063509 (1999), arXiv:astro-ph/9901268.

[100] Florian Kühnel, Cornelius Rampf, and Marit Sandstad, "Effects of Critical Collapse on Primordial Black-Hole Mass Spectra," Eur. Phys. J. C **76**, 93 (2016), arXiv:1512.00488 [astro-ph.CO].

[101] Kristjan Kannike, Luca Marzola, Martti Raidal, and Hardi Veermäe, "Single Field Double Inflation and Primordial Black Holes," JCAP **09**, 020 (2017), arXiv:1705.06225 [astro-ph.CO].

[102] Jane H. MacGibbon, "Quark and gluon jet emission from primordial black holes. 2. The Lifetime emission," Phys. Rev. D **44**, 376–392 (1991).

[103] Markus R. Mosbech and Zachary S. C. Picker, "Effects of Hawking evaporation on PBH distributions," SciPost Phys. **13**, 100 (2022), arXiv:2203.05743 [astro-ph.HE].

[104] Jérôme Martin, Theodoros Papanikolaou, and Vincent Vennin, "Primordial black holes from the preheating instability in single-field inflation," JCAP **01**, 024 (2020), arXiv:1907.04236 [astro-ph.CO].

[105] Junsong Cang, Yu Gao, and Yin-Zhe Ma, "21-cm constraints on spinning primordial black holes," JCAP **03**, 012 (2022), arXiv:2108.13256 [astro-ph.CO].

[106] Marc Davis, George Efstathiou, Carlos S. Frenk, and Simon D. M. White, "The Evolution of Large Scale Structure in a Universe Dominated by Cold Dark Matter," Astrophys. J. **292**, 371–394 (1985).

[107] Marijn Franx, Garth Illingworth, and Tim de Zeeuw, "The Ordered Nature of Elliptical Galaxies: Implications for Their Intrinsic Angular Momenta and Shapes," Astrophys. J. **383**, 112 (1991).

[108] Julio F. Navarro, Carlos S. Frenk, and Simon D. M. White, "The Structure of cold dark matter halos," Astrophys. J. **462**, 563–575 (1996), arXiv:astro-ph/9508025.

[109] James Binney and Leong Khim Wong, "Modelling the Milky Way's globular cluster system," Mon. Not. Roy. Astron. Soc. **467**, 2446–2457 (2017), arXiv:1701.06995 [astro-ph.GA].

[110] Lorenzo Posti and Amina Helmi, "Mass and shape of the Milky Way's dark matter halo with globular clusters from Gaia and Hubble," Astron. & Astrophys. **621**, A56 (2019), arXiv:1805.01408 [astro-ph.GA].

[111] P. F. de Salas, K. Malhan, K. Freese, K. Hattori, and M. Valluri, "On the estimation of the Local Dark Matter Density using the rotation curve of the Milky Way," JCAP **10**, 037 (2019), arXiv:1906.06133 [astro-ph.GA].

[112] Xiaowei Ou, Anna-Christina Eilers, Lina Necib, and Anna Frebel, "The dark matter profile of the Milky Way inferred from its circular velocity curve," Mon. Not. Roy. Astron. Soc. **528**, 693–710 (2024), arXiv:2303.12838 [astro-ph.GA].

[113] Prajwal Raj Kafle, Sanjib Sharma, Geraint F. Lewis, and Joss Bland-Hawthorn, "On the Shoulders of Giants: Properties of the Stellar Halo and the Milky Way Mass Distribution," Astrophys. J. **794**, 59 (2014), arXiv:1408.1787 [astro-ph.GA].

[114] M. Weber and W. de Boer, "Determination of the local dark matter density in our Galaxy," Astron. & Astrophys. **509**, A25 (2010), arXiv:0910.4272 [astro-ph.CO].

[115] J. I. Read, "The local dark matter density," J. Phys. G Nucl. Phys. **41**, 063101 (2014), arXiv:1404.1938 [astro-ph.GA].

[116] D.G. Cerdeño and A.M. Greene, *Particle Dark Matter: Observations, Models and Searches* (Cambridge University Press, Cambridge, UK; New York, 2010).

[117] K. Choi, Carsten Rott, and Yoshitaka Itow, "Impact of the dark matter velocity distribution on capture rates in the Sun," JCAP **05**, 049 (2014), arXiv:1312.0273 [astro-ph.HE].

[118] K. S. Oh, "Velocity Distribution of Dark Matter Galactic Halo," J. Korean Astron. Soc. **30**, 95–106 (1997).

[119] Katharena Christy, Jason Kumar, and Louis E. Strigari, "Dark matter velocity distributions: Comparing numerical simulations to analytic results," Phys. Rev. D **109**, 063016 (2024), arXiv:2309.01979 [astro-ph.CO].

[120] Shuyu Wang, Lina Necib, Alexander P. Ji, Xiaowei Ou, Mariangela Lisanti, Mithi A. C. de los Reyes, Allison L. Strom, and Mimi Truong, "High-resolution Chemical Abundances of the Nyx Stream," Astrophys. J. **955**, 129 (2023), arXiv:2210.15013 [astro-ph.GA].

[121] Thomas Donlon, II, Heidi Jo Newberg, Bokyoung Kim, and Sebastien Lépine, "The Local Stellar Halo is Not Dominated by a Single Radial Merger Event," Astrophys. J. Lett.sha **932**, L16 (2022), arXiv:2110.11465 [astro-ph.GA].

[122] T. Bruch, J. Read, L. Baudis, and G. Lake, "Detecting the Milky Way's Dark Disk," Astrophys. J. **696**, 920–923 (2009), arXiv:0804.2896 [astro-ph].

[123] M. Aguilar *et al.* (AMS), "Temporal Structures in Positron Spectra and Charge-Sign Effects in Galactic Cosmic Rays," Phys. Rev. Lett. **131**, 151002 (2023).

[124] F. J. Lowes and B. Duka, "Magnetic multipole moments (Gauss coefficients) and vector potential given by an arbitrary current distribution," Earth, Planets and Space **63**, i–vi (2011).

[125] P. Alken *et al.*, "International Geomagnetic Reference Field: the thirteenth generation," Earth, Planets and Space **73**, 49 (2021).

[126] Loïc Huder, Nicolas Gillet, Christopher C. Finlay, Magnus D. Hammer, and Hervé Tchoungui, "COV-OBS.x2: 180 years of geomagnetic field evolution from ground-based and satellite observations," Earth, Planets and Space **72**, 160 (2020).

[127] Monika Korte and Raimund Muscheler, "Centennial to millennial geomagnetic field variations," Journal of Space Weather and Space Climate **2**, 08 (2012).

[128] S. Panovska, M. Korte, and C. G. Constable, "One Hundred Thousand Years of Geomagnetic Field Evolution," Reviews of Geophysics **57**, 1289–1337 (2019).

[129] Stuart Gaffin, "Analysis of scaling in the geomagnetic polarity reversal record," Physics of the Earth and Planetary Interiors **57**, 284–290 (1989).

[130] J. D. Phillips and A. Cox, "Spectral analysis of geomagnetic reversal time scales." Geophysical Journal **45**, 19–33 (1976).

[131] Carl Størmer, *The Polar Aurora* (Oxford University Press, Oxford, UK, 1955).

[132] B. T. Kress, M. K. Hudson, R. S. Selesnick, C. J. Mertens, and M. Engel, "Modeling geomagnetic cutoffs for space weather applications," Journal of Geophysical Research (Space Physics) **120**, 5694–5702 (2015).

[133] D. F. Smart and M. A. Shea, "A review of geomagnetic cutoff rigidities for earth-orbiting spacecraft," Advances in Space Research **36**, 2012–2020 (2005).

[134] M. Aguilar *et al.* (AMS), "Towards Understanding the Origin of Cosmic-Ray Positrons," Phys. Rev. Lett. **122**, 041102 (2019).

[135] V. Bindi *et al.*, "The scintillator detector for the fast trigger and time-of-flight (TOF) measurement of the space experiment AMS-02," Nucl. Instrum. Meth. A **623**, 968–981 (2010).

[136] F. Giovacchini (AMS02-RICH), "Performance in space of the AMS-02 RICH detector," Nucl. Instrum. Meth. A **766**, 57–60 (2014).

[137] I. B. Khriplovich and D. L. Shepelyansky, "Capture of dark matter by the Solar System," Int. J. Mod. Phys. D **18**, 1903–1912 (2009), arXiv:0906.2480 [astro-ph.SR].

[138] Fabio Capela, Maxim Pshirkov, and Peter Tinyakov, "Constraints on Primordial Black Holes as Dark Matter Candidates from Star Formation," Phys. Rev. D **87**, 023507 (2013), arXiv:1209.6021 [astro-ph.CO].

[139] Fabio Capela, Maxim Pshirkov, and Peter Tinyakov, "Constraints on primordial black holes as dark matter candidates from capture by neutron stars," Phys. Rev. D **87**, 123524 (2013), arXiv:1301.4984 [astro-ph.CO].

[140] Yoann Génolini, Pasquale Serpico, and Peter Tinyakov, "Revisiting primordial black hole capture into neutron stars," Phys. Rev. D **102**, 083004 (2020), arXiv:2006.16975 [astro-ph.HE].

[141] Benjamin V. Lehmann, Olivia G. Ross, Ava Webber, and Stefano Profumo, "Three-body capture, ejection, and the demographics of bound objects in binary systems," Mon. Not. Roy. Astron. Soc. **505**, 1017–1028 (2021), arXiv:2012.05875 [astro-ph.SR].

[142] Benjamin V. Lehmann, Ava Webber, Olivia G. Ross, and Stefano Profumo, "Capture of primordial black holes in extrasolar systems," JCAP **08**, 079 (2022), arXiv:2205.09756 [astro-ph.EP].

[143] Roberto Caiozzo, Gianfranco Bertone, and Florian Kühnel, "Revisiting primordial black hole capture by neutron stars," JCAP **07**, 091 (2024), arXiv:2404.08057 [astro-ph.HE].

[144] Peter Tinyakov, "The Asteroid Mass Window," (2025) arXiv:2406.03114 [astro-ph.CO].

[145] Marc Oncins, Jordi Miralda-Escudé, Jordi L. Gutiérrez, and Pilar Gil-Pons, "Primordial black holes capture by stars and induced collapse to low-mass stellar black holes," Mon. Not. Roy. Astron. Soc. **517**, 28–37 (2022), arXiv:2205.13003 [astro-ph.GA].

[146] Earl P. Bellinger, Matt E. Caplan, Taeho Ryu, Deepika Bollimpalli, Warrick H. Ball, Florian Kühnel, R. Farmer, S. E. de Mink, and Jørgen Christensen-Dalsgaard, "Solar Evolution Models with a Central Black Hole," Astrophys. J. **959**, 113 (2023), arXiv:2312.06782 [astro-ph.SR].

[147] Matthew E. Caplan, Earl P. Bellinger, and Andrew D. Santarelli, "Is there a black hole in the center of the Sun?" Astrophys. Space Sci. **369**, 8 (2024), arXiv:2312.07647 [astro-ph.SR].

[148] Vitorio A. De Lorenci, David I. Kaiser, Patrick Peter, Lucas S. Ruiz, and Noah E. Wolfe, "Gravitational wave signals from primordial black holes orbiting solar-type stars," (2025), arXiv:2504.07517 [gr-qc].

[149] Almog Yalinewich and Matthew E. Caplan, "Crater Morphology of Primordial Black Hole Impacts," Mon. Not. Roy. Astron. Soc.: Letters **505**, L115–L119 (2021), arXiv:2104.00033 [astro-ph].

[150] Andrew D. Santarelli, Matthew E. Caplan, and Nevin T. Smith, "Possible constraints on asteroid-mass primordial black holes from Solar system cratering," Mon. Not. Roy. Astron. Soc. **538**, 108–113 (2025).

[151] Italian Space Agency, "GeoMagSphere Online calculator," **v.2.1**.

[152] P. Bobik, G. Boella, M. J. Boschini, M. Gervasi, D. Grandi, K. Kudela, S. Pensotti, and P. G. Rancoita, "Magnetospheric transmission function approach to disentangle primary from secondary cosmic ray fluxes in the penumbra region," Journal of Geophysical Research (Space Physics) **111**, A05205 (2006).

[153] M. J. Boschini *et al.*, "Geomagnetic Backtracing: A comparison of Tsyganenko 1996 and 2005 External Field models with AMS-02 data," in *33rd International Cosmic Ray Conference* (2013) p. 1148, arXiv:1307.5192 [astro-ph.IM].

[154] Davide Grandi *et al.*, "Trajectory reconstruction in the Earth Magnetosphere using TS05 model and evaluation of geomagnetic cutoff in AMS-02 data," PoS **ICRC2015**, 116 (2016).

[155] F. Javier Pavón-Carrasco and Angelo De Santis, "The south atlantic anomaly: The key for a possible geomagnetic reversal," Frontiers in Earth Science **4** (2016), 10.3389/feart.2016.00040.

[156] Andreas Shalchi, *Nonlinear Cosmic Ray Diffusion Theories*, Astrophysics and Space Science Library, Vol. 362 (Springer, 2009).

[157] F. Effenberger, H. Fichtner, K. Scherer, S. Barra, J. Kleimann, and R. D. Strauss, "A Generalized Diffusion Tensor for Fully Anisotropic Diffusion of Energetic Particles in the Heliospheric Magnetic Field," ApJ **750**, 108 (2012).

[158] R. A. Burger, T. P. J. Krüger, M. Hitge, and N. E. Engelbrecht, "A Fisk-Parker Hybrid Heliospheric Magnetic Field with a Solar-Cycle Dependence," ApJ **674**, 511 (2008).

[159] B. Alpat *et al.*, "The internal alignment and position resolution of the AMS-02 silicon tracker determined with cosmic-ray muons," NIM-A **613**, 207–217 (2010).

[160] AMS Collaboration, M. Aguilar, *et al.*, "Electron and Positron Fluxes in Primary Cosmic Rays Measured with the Alpha Magnetic Spectrometer on the International Space Station," Phys. Rev. Lett. **113**, 121102 (2014).

[161] Alessio Ubaldi and Maura Graziani, "Charge Resolution Study on AMS-02 Silicon Layer-0 Prototype," Instruments **7**, 45 (2023).

[162] I. V. Moskalenko and A. W. Strong, "Production and propagation of cosmic ray positrons and electrons," Astrophys. J. **493**, 694–707 (1998), arXiv:astro-ph/9710124.

[163] Oscar Adriani *et al.* (PAMELA), "An anomalous positron abundance in cosmic rays with energies 1.5-100 GeV," Nature **458**, 607–609 (2009), arXiv:0810.4995 [astro-ph].

[164] S. Abdollahi *et al.* (Fermi-LAT), "Cosmic-ray electron-positron spectrum from 7 GeV to 2 TeV with the Fermi Large Area Telescope," Phys. Rev. D **95**, 082007 (2017), arXiv:1704.07195 [astro-ph.HE].

[165] Hong-Bo Jin, Yue-Liang Wu, and Yu-Feng Zhou, "Astrophysical background and dark matter implication based on latest AMS-02 data," Astrophys. J. **901**, 80 (2020), arXiv:1701.02213 [hep-ph].

[166] Dan Hooper, Pasquale Blasi, and Pasquale Dario Serpico, "Pulsars as the Sources of High Energy Cosmic Ray Positrons," JCAP **01**, 025 (2009), arXiv:0810.1527 [astro-ph].

[167] Jamie S. Rankin, Veronica Bindi, Andrei M. Bykov, Alan C. Cummings, Stefano Della Torre, Vladimir Florinski, Bernd Heber, Marius S. Potgieter, Edward C. Stone, and Ming Zhang, "Galactic Cosmic Rays Throughout the Heliosphere and in the Very Local Interstellar Medium," Space Sci. Rev. **218**, 42 (2022).

[168] J. S. Rankin, E. C. Stone, A. C. Cummings, D. J. McComas, N. Lal, and B. C. Heikkila, "Galactic Cosmic-Ray Anisotropies: Voyager 1 in the Local Interstellar Medium," Astrophys. J. **873**, 46 (2019), arXiv:1905.11990 [physics.space-ph].

[169] V. V. Mikhailov and S. A. Voronov (PAMELA), "Spectra of Electrons and Positrons with Energies above 50 MeV, According to Data from the PAMELA Experiment," Bull. Russ. Acad. Sci. Phys. **85**, 1036–1038 (2021).

[170] William DeRocco and Peter W. Graham, "Constraining Primordial Black Hole Abundance with the Galactic 511 keV Line," Phys. Rev. Lett. **123**, 251102 (2019), arXiv:1906.07740 [astro-ph.CO].

[171] Ranjan Laha, "Primordial Black Holes as a Dark Matter Candidate Are Severely Constrained by the Galactic Center 511 keV γ -Ray Line," Phys. Rev. Lett. **123**, 251101 (2019), arXiv:1906.09994 [astro-ph.HE].